Open access • Journal Article • DOI:10.1021/ACS.INORGCHEM.5B02920

Spin State Energetics and Oxyl Character of Mn-Oxo Porphyrins by Multiconfigurational ab Initio Calculations: Implications on Reactivity — Source link

Sergio Augusto Venturinelli Jannuzzi, Sergio Augusto Venturinelli Jannuzzi, Quan Manh Phung, Alex Domingo ...+2 more authors

Institutions: Katholieke Universiteit Leuven, State University of Campinas

Published on: 22 Feb 2016 - Inorganic Chemistry (American Chemical Society)

Topics: Triplet state and Ab initio

Spin-State Energetics and Oxyl Character of Mn-Oxo Porphyrins by Multiconfigurational ab initio Calculations: Implications on Reactivity

Sergio Augusto Venturinelli Jannuzzi,[†,‡] Quan Manh Phung,[‡] Alex Domingo,[‡] André Luiz Barboza Formiga,[†] and Kristine Pierloot[*,‡]

Institute of Chemistry, P.O. Box 6154, University of Campinas – UNICAMP, 13083-970, Campinas, SP, Brazil, and Department of Chemistry, KU Leuven, Celestijnenlaan 200F, B-3001 Leuven, Belgium

E-mail: Kristin.Pierloot@chem.kuleuven.be

[*]To whom correspondence should be addressed

[†]Institute of Chemistry, P.O. Box 6154, University of Campinas – UNICAMP, 13083-970, Campinas, SP, Brazil

[‡]Department of Chemistry, KU Leuven, Celestijnenlaan 200F, B-3001 Leuven, Belgium

Abstract

Important electromeric states in manganese-oxo porphyrins $MnO(P)^+$ and $MnO(PF_4)^+$ (porphyrinato or *meso*-tetrafluoroporphyrinato) have been investigated with correlated ab initio methods (CASPT2, RASPT2), focusing on their possible role in multi-state reactivity patterns in oxygen transfer (OAT) reactions. Due to the lack of oxyl character, the Mn^V singlet ground state is kinetically inert. OAT reactions should therefore rather proceed through thermally accessible triplet and quintet states that have a more pronounced oxyl character. Two states have been identified as possible candidates: a Mn^V triplet state and a $Mn^{IV}O(L^\bullet a_{2u})^+$ quintet state. The latter state is high-lying in $MnO(P)^+$ but is stabilized by the substitutions of H by F at the *meso* carbons (where the a_{2u} orbital has a significant amplitude). Oxyl character and Mn–O bond weakening in these two states stems from the fact that the Mn–O π^* orbitals become singly (triplet) or doubly occupied (quintet). Moreover, an important role for the reactivity of the triplet state is also likely to be played by the π bond that has an empty π^* orbital, because of the manifest diradical character of this π bond, revealed by the CASSCF wave function. Interestingly, the diradical character of this bond increases when the Mn–O bond is stretched, while the singly occupied π^* orbital looses its oxygen radical contribution. The RASPT2 results were also used as a benchmark for the description of excited state energetics and Mn–O oxyl character with a wide range of pure and hybrid density functionals. With the latter functionals both the $Mn^V \rightarrow Mn^{IV}$ promotion energy and the diradical character of the π bond (with empty π^*) are found to be extremely dependent on the contribution of exact exchange. For this reason, pure functionals are to be preferred.

Introduction

Both iron- and manganese-oxo species play an important catalytic role in biological processes involving oxygen activation and transfer. The cytochrome P450s are a multifunctional family of proteins that are highly specialized in effective oxygen transfer to organic substrates.[1–4] The oxygen atom transfer (OAT) reaction involves the so-called Compound I, a high-valent iron-oxo porphyrin with a strong oxidant character. Manganese-oxo species have a key role in oxygen transfer reactions in biological systems as well, *e.g.* in the oxidation of water to molecular oxygen in photosystem II.[5] Inspired by the successful catalytic role of these bioinorganic species in living organisms, iron porphyrins and their manganese counterparts have been extensively studied as suitable catalysts for *in vitro* oxidation reactions, and synthetic analogues have been developed that are able to reproduce most OAT reactions observed in natural enzymes.[6–10]

The high-valent Mn complex responsible for OAT has been characterized experimentally as a diamagnetic manganese(V)-oxo porphyrin species ($Mn^{V}OP$).[11–13] In alkaline conditions this complex shows a remarkable stability, which was attributed to its low-spin (S=0) d^2 ground state character.[12,14–16] Such a ground state electronic structure was confirmed by calculations based on Density Functional Theory (DFT) employing pure generalized gradient functionals (GGA).,[17–19] from which it was also concluded that the reason behind the inertness towards OAT of this singlet ($Mn^{V}OP$) species is the absence of significant oxyl character in the Mn–O axial oxygen.[17,18]

A qualitative molecular orbital (MO) diagram of $Mn^{V}OP$ is provided in Figure 1. In the ground state the Mn($3d^2$) center has its two 3d electrons paired in one non-bonding 3d-like MO ($3d_\delta$). The Mn–O σ bond is formed from bonding/antibonding combinations of Mn d_{z^2} and O p_z (σ_z, σ_z^*) whereas a double π bond is formed from bonding/antibonding MO pairs between Mn (d_{xz}, d_{yz}) and O (p_x,p_y). Of these six MOs, the three bonding combinations σ_z, (π_{xz}, π_{yz}) (not shown in Figure 1) are doubly occupied, whereas the corresponding antibonding orbitals σ_z^*,(π_{xz}^*, π_{yz}^*) remain empty. This gives rise to a very strong (triple) Mn–O

bond, which is short and kinetically stable, and lacks oxygen radical character. As proposed by Jin and Groves[12] release of oxygen from $Mn^{V}OP^{+}$ should therefore rather proceed via thermally accessible reactive high-spin (HS, triplet or quintet) state(s), by transfer of one or two electrons from either $3d_{\delta}$ or a porphyrin π orbital (or both, see Figure 1) into the $(\pi^{*}_{xz}, \pi^{*}_{yz})$ orbitals, thus weakening the Mn–O bond and enhancing its oxyl character. The fact that multiple low-lying states may be involved in and affect the reactivity of OAT ractions is of course not unprecedented, and has been extensively illustrated by Shaik *et al.* for cytochrome P450 enzymes.[2]

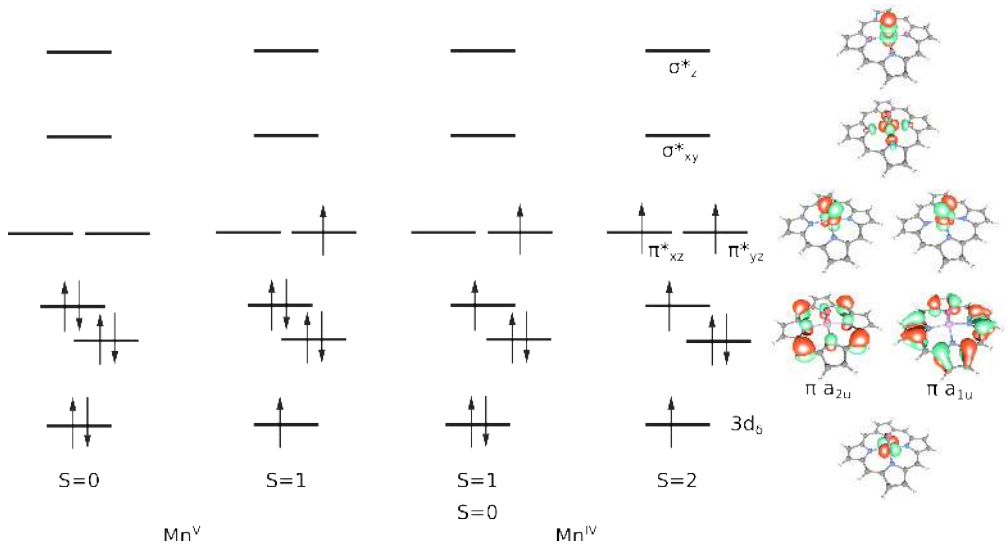

Figure 1: Electronic structure of low-lying states of Mn-oxo porphyrins considered in this work. Mn^{V} d^2 states have both porphyrin π a_{2u} and π a_{1u} orbitals doubly occupied. One set of three Mn^{IV} d^3 states has π a_{2u} singly occupied and the second set of Mn^{IV} states has π a_{1u} singly occupied, making a total of eight states.

If OAT by $Mn^{V}OP$ is triggered by transition to low-lying HS states, then reactivity is dependent on the relative energy of such states with respect to the singlet ground state. This opens the way to control the oxygen transfer by external stimuli. The catalytic activity of such complexes could be not only defined upon synthesis, by creating their molecular structure, but also fine tuned in the reacting environment. A nice illustration of this was provided in a study of Eisenstein *et al.*, based on DFT/BP86 calculations.[17,18] Here, a rationalization was provided for the role played by the environmental pH on the OAT reactivity of $Mn^{V}OP$,

highlighting the effect of ligand coordination *trans* to the Mn-O bond on the energy gap between the singlet and the lowest HS states. In alkaline conditions, the *trans* ligand is OH^-, whereas a decrease in pH will favour coordination of H_2O instead. With DFT/BP86, substitution of OH^- by H_2O gives rise to a stabilization of the lowest quintet state from 22.4 to 12.1 kcal mol^{-1} and of the triplet state from 9.2 to 4.7 kcal mol^{-1}, thus making at least the latter state thermally accessible. As such, lowering the pH should, by protonating the OH^- ligand, turn an inert singlet $Mn^{V}OP$ into a catalytically active species, conform with the experimentally observed increase of the OAT rate constant with increasing acidity.[15,19]

Although the above example clearly illustrates the power of DFT for the description and rationalization of these important bio-inorganic catalytic processes, DFT failures associated with the description of relative energies of different metal oxidation and spin states, and their functional dependence in particular, have also been amply illustrated in the literature.[20–23] In the specific case of manganese-oxo porphyrins, two previous DFT studies indicated that the popular B3LYP functional fails to reproduce the diamagnetic ground state of *e.g.* the $MnO(P)^+$ complex with a H_2O axial ligand, which is rather predicted to be a (strongly spin contaminated) $Mn^{V}OP^+$ triplet state[24] or a $Mn^{IV}OP^{\bullet+}$ quintet state[25] (see Figure 1) The S=0 state, i.e. the experimentally observed and theoretically predicted ground state with BP86, is found with B3LYP at 9.7–13.2 kcal mol^{-1} above the ground state. The inferior behaviour of B3LYP for this particular case is striking in the sense that the same functional has been extensively used with considerable success for the description of the full catalytic cycle of cytochrome P450.[2] In a previous benchmarking study on iron-oxo porphyrins $FeOP^+$ and FeOPCl we found that B3LYP can provide a reasonable description of the relative spin state energetics of different low-lying $Fe^{IV}OP^{\bullet+}$ states, but is much less accurate in describing electron transfer between the metal and the porphyrin.[26] Another painful area in the behavior of DFT for these high valent manganese-oxo systems concerns the functional dependence in the prediction of oxyl radical character, which is a crucial factor for oxidative activity. Hybrid and non-hybrid functionals were found to provide completely

different descriptions of the spin density distribution in the manganese oxo bond, thus also giving very different qualitative descriptions of the oxidation reactivity.[24] On the whole, it is clear that benchmarking of available DFT functionals against high-level correlated methods is necessary to establish the optimal functional and estimate the error bars, before any quantitative results may be obtained from DFT regarding the description of the actual reactions with different substrates.

In the present study we aim to provide a quantitative description of the relative energies of low-lying electromeric states in two model systems, Mn-oxo porphyrinato ($MnO(P)^+$) and *meso*-tetrafluoroporphyrinato ($MnO(PF_4)^+$), by means of the multiconfigurational ab initio methods CASPT2 (complete active space second-order perturbation theory)[27] and its generalization to RASPT2 (restricted active space second-order perturbation theory),[28] which have already been extensively used on other heme and heme-related complexes.[23,26,29–31] The oxyl character of the Mn–O bond in each of the calculated states will be assessed by an analysis of the multiconfigurational wave function and the associated spin density distribution. The results are used to benchmark the excited state energetics and spin density obtained from an extensive series of available DFT functionals. This benchmark will be useful for future investigations of the reactivity of larger systems based on Mn-oxo porphyrins, which might be too demanding for the CASPT2/RASPT2 methods. Our study includes all possible low-lying electromeric states in both molecules, that is the Mn^V d^2 singlet and triplet states, and the quintet, triplet, and singlet Mn^{IV} states with either one of the HOMO π orbitals of the porphyrin, a_{1u} or a_{2u} (where we use the familiar D_{4h} notation) singly occupied.

Computational Details

Structure optimizations

For each electronic state, a full structure optimization was performed in vacuum, making use of DFT calculations with the PBE0 functional,[32,33] and employing def2-TZVP basis

sets.[34] The choice of the PBE0 functional was based on our previous experience with similar complexes (*i.e.* manganese-oxo corroles and corrolazines).[31] The calculations were performed making use of the unrestricted DFT approach. For the Mn^V singlet ground state this resulted in a pure (S=0) restricted solution, whereas the Mn^V triplet state was found to be excessively spin contaminated. The spin contamination is related to the strong diradical character of the Mn–O bond in this triplet state (further discussed below) giving rise to an exceptionally large Mn–O bond distance in the UPBE0 structure (see Table S1 and Figure S1a). In order to circumvent this problem, the structure of the Mn^V (S=1) state was instead obtained with ROPBE0. Geometry optimizations for the Mn^{IV} quintet and triplet states of $MnO(P)^+$ were also performed with ROPBE0. However, since the ROPBE0 and UPBE0 structures for these states were found to be close, the UPBE0 structures were used in further calculations of the spin state energetics, as described below. The UPBE0 calculations are performed with the TURBOMOLE v6.4 package,[35] whereas for the ROPBE0 structure calculations we used the MOLPRO v2012 package.[36]

The geometry optimizations are performed under the C_{2v} symmetry point group. The character of the stationary points on the potential energy surface was verified by frequency calculations. The maximum symmetry that could be displayed by both $MnO(P)^+$ and $MnO(PF_4)^+$ is C_{4v}. However, most of the calculated structures showed a distortion to C_{2v}, either with a ruffled (with the σ_v planes between the N–Mn–N bond) or saddled (with the σ_v planes containing the Mn–N bonds) porphyrin core. Both ruffled and saddled C_{2v} structures were optimized for all states. The lowest energy structures are reported in the Supplementary Information (Table S1). For the triplet and open-shell singlet states, containing one electron in the Mn–O π^* shell, the parent state in C_{4v} symmetry is $^{3,1}E$, and the distortion to C_{2v} is (first-order) Jahn-Teller driven. Two equivalent distortions are possible, giving rise to a $^3B_1$ and $^3B_2$ state in C_{2v}. As both energy minima are equi-energetic, only the $^3B_1$ state is reported. The structures of the quintet states, $^5A_1(Mn^{IV}O(L^{\bullet}a_{1u})^+)$ and $^5A_2(Mn^{IV}O(L^{\bullet}a_{2u})^+)$ (with L = P or PF_4) do reveal C_{4v} symmetry. However, the closed-

shell Mn^V $^1A_1$ state is found to be quite strongly distorted. For the two Mn^V states, $^1A_1$ and $^3B_1$, we obtained ruffled structures, while the Mn^{IV} $^{3,1}B_1$ structures are saddled. It should be noted though that for $MnO(P)^+$ the reported C_{2v} structures of the $Mn^{IV}O(P^\bullet a_{2u})^+$ states are not structural minima. They have one imaginary frequency that lowers their symmetry to C_2. Following the path connected to the imaginary frequency leads to the lower-lying $Mn^{IV}O(P^\bullet a_{1u})^+$ states. As such, at the DFT level the $Mn^{IV}O(P^\bullet a_{2u})^+$ states are in fact transition states connecting two $Mn^{IV}O(P^\bullet a_{1u})^+$ minima. An overview of the different states and their (dominant) configuration is provided in Table 1.

Table 1: Dominant electronic configuration of relevant states investigated for $MnO(L)^+$, with L=P,PF_4.

		$Mn(3d_\delta)^a$	$P(\pi a_{1u})$	$P(\pi a_{2u})$	π^*_{xz}	π^*_{yz}
$^1Mn^VO(L)$	$^1A_1$	$\uparrow\downarrow$	$\uparrow\downarrow$	$\uparrow\downarrow$		
$^3Mn^VO(L)$	$^3B_1$	$\uparrow$	$\uparrow\downarrow$	$\uparrow\downarrow$		$\uparrow$
$^5Mn^{IV}O(L^\bullet a_{2u})$	$^5A_2$	$\uparrow$	$\uparrow\downarrow$	$\uparrow$	$\uparrow$	$\uparrow$
$^3Mn^{IV}O(L^\bullet a_{2u})$	$^3B_1$	$\uparrow\downarrow$	$\uparrow\downarrow$	$\uparrow$	$\uparrow$	
$^1Mn^{IV}O(L^\bullet a_{2u})$	$^1B_1$ [b]	$\uparrow\downarrow$	$\uparrow\downarrow$	$\downarrow$	$\uparrow$	
$^5Mn^{IV}O(L^\bullet a_{1u})$	$^5A_2$	$\uparrow$	$\uparrow$	$\uparrow\downarrow$	$\uparrow$	$\uparrow$
$^3Mn^{IV}O(L^\bullet a_{1u})$	$^3B_1$	$\uparrow\downarrow$	$\uparrow$	$\uparrow\downarrow$		$\uparrow$
$^1Mn^{IV}O(L^\bullet a_{1u})$	$^1B_1$ [b]	$\uparrow\downarrow$	$\downarrow$	$\uparrow\downarrow$		$\uparrow$

[a] $3d_\delta$ denotes the non-bonding MO localized on Mn, whose main character is $Mn(3d_{x^2-y^2})$ or $Mn(3d_{xy})$ depending on the molecular symmetry.

[b] This is the single determinant calculated by UDFT, which is in fact an equal mixture of $^1B_1$ and $^3B_1$. In the CASSCF and RASSCF calculations the pure $^1B_1$ wave function is calculated instead.

For the lowest lying states, *i.e.* the Mn^V $^1A_1$ and Mn^V $^3B_1$ states of both complexes, as well as the Mn^{IV} $^5A_2(a_{2u})$ state of $MnO(PF_4)^+$, the Mn–O distance was also optimized at the CASPT2 level. To this end, partially constrained structure optimizations were performed with PBE0 (UDFT for $^1A_1$ and $^5A_2$, RODFT for $^3B_1$), for Mn–O distances ranging between 1.4 and 2.0 Å. For each of the structures, single-point CASPT2 calculations were performed to obtain the CASPT2 Mn–O dissociation curves. The CASPT2 calculations were carried out according to the description given below, and including solvent effects.

Calculations of spin state energetics

The resulting DFT/PBE0 structures are used in two subsequent stages of this study (i) estimation of the spin state energetics of the complexes through CASPT2 and RASPT2 electronic structure calculations and (ii) benchmarking a set of DFT functionals against the spin state energetics obtained at the RASPT2 level.

CASPT2 and RASPT2 calculations

Single point CASSCF/CASPT2[27] and RASSCF/RASPT2[28] calculations using the DFT/PBE0 molecular structures were performed with the MOLCAS 7.9 package.[37] We use a basis set of the ANO-RCC[38] type contracted to [7s6p5d2f2g1h] for Mn; [4s3p2d1f] for C, N, O and F; and [3s1p] for H.[39] Scalar-relativistic effects are treated by means of the second-order Douglas-Kroll-Hess Hamiltonian.[40] The two-electron integrals are decomposed by means of the Cholesky technique with a threshold of 10^{-6} hartree.[41] Solvation effects are introduced in the model through a polarizable continuum model (PCM)[42] with a dielectric constant of 53.54 that corresponds to a mixture of water and acetonitrile.[43] All CASPT2 and RASPT2 calculations use the standard IPEA shift value of 0.25 hartree for the zero-order second-order Hamiltonian[44] and an imaginary level shift[45] of 0.1 hartree to prevent weak intruder states. All valence electrons as well as the metal (3s,3p) semi-core electrons are correlated at the CASPT2 and RASPT2 levels.

The active space is chosen based on established procedures for transition metal compounds.[46–48] We define a complete active space of 14 electrons in 16 to 18 orbitals, denoted as CAS(14,N) with N = 16, 17 or 18. In all cases, the CAS takes into account the static correlation of the Mn 3d shell, the covalency of the Mn–O bond and the σ-donation from the porphyrin by including the following four pairs of bonding/antibonding MOs, Mn($3d_{z^2}$)–O($2p_z$) (σ_z,σ_z^*), Mn($3d_{xz}$)–O($2p_x$) (π_{xz},π_{xz}^*), Mn($3d_{yz}$)–O($2p_y$) (π_{yz},π_{yz}^*) and Mn($3d_{xy}$)–P(σ_{xy}) (σ_{xy},σ_{xy}^*); as well as the remaining non-bonding Mn($3d_\delta$) orbital. Additionally, the active space also includes a set of four π MOs localized on the porphyrin to

allow the electron transition between Mn and the porphyrinato ligand. This is the so-called *Gouterman set* and comprises the two high-lying occupied π orbitals P(π a_{1u}) and P(π a_{2u}), and the correlating P(π^* e_g) orbitals. Finally, we incorporate the double-shell effect of both Mn and O by adding the O($3p_x$) and O($3p_y$) orbitals plus a maximum of three Mn(4d) MOs, namely $4d_\delta$, $4d_{xz}$ and $4d_{yz}$. The variable size of the CAS depends on the magnitude of the double shell effect on the metal centre, which is proportional to the occupation of the Mn(3d)-like MOs and hence, is affected by the spin and oxidation state of Mn. The $^1Mn^VO(L)$ singlet state is described with the smaller CAS(14,16) and has virtual $4d_{xz}$ and $4d_{yz}$ MOs as both π^*_{xz} and π^*_{yz} are unoccupied. The states $^3Mn^VO(L)$ and $^{1,3}Mn^{IV}O(L^\bullet)$ that have a larger number of open shells require a larger CAS(14,17) and the quintets $^5Mn^{IV}O(L^\bullet)$ use the largest CAS(14,18) with both $4d_{xz}$ and $4d_{yz}$ MOs active. The active orbitals are displayed in Figure 2.

Previous studies on the low-lying states of iron-oxo porphyrins[26] and manganese-oxo corroles and corrolazines[31] show that more porphyrin π/π^* active orbitals are needed to obtain an accurate description of the spin-states with a radical porphyrin. Thus, we built a restricted active space (RAS) with 28 electrons in 28 to 30 orbitals (Figure 2) that expands the CAS(14,N) with a selection of additional P(π) and P(π^*) orbitals. The resulting RAS contains all P(π)/P(π^*) orbitals except four pairs localized on the eight pyrrole β carbons. The RAS is divided in three sub-spaces (RAS1, RAS2 and RAS3) and capacitates us to work with such large amount of active orbitals by limiting the number of excitations allowed between the sub-spaces. The molecular orbitals are optimized with a RAS2 sub-space including three pairs of bonding/antibonding Mn(3d)–O(2p) orbitals (*i.e.* σ_z, σ^*_z, π_{xz}, π^*_{xz}, π_{yz} and π^*_{yz}) and all remaining singly occupied orbitals. As we discussed in a previous study,[49] the accuracy of RASPT2 on transition metal complexes is increased by including the bonding/antibonding metal–ligand combinations in the same RAS sub-space, as otherwise the coupling element between these two orbitals in the Fock matrix would be neglected in the RASPT2 treatment. The active orbitals nearly doubly occupied are kept in RAS1 and the

nearly unoccupied are in RAS3, allowing up to double excitations out of RAS1 and into RAS3 sub-spaces. In a second calculation, the RAS2 sub-space was further extended with the bonding/antibonding σ_{xy} and σ^*_{xy} orbitals. However, this gives rise to a very large number of configurations, rendering any further optimization of the orbitals prohibitive. Therefore, only the optimization of the CI coefficients was done in this second step, again allowing up to double excitations out of RAS1 and into RAS3.

DFT calculations

For $MnO(P)^+$ a benchmark study was performed of the relative energies of the different electromeric states obtained from different DFT functionals. To this end, single point calculations were performed making use of the structures obtained from PBE0 (see above). We tested a broad range of functionals covering members of the hybrid and non-hybrid families. Those include pure GGAs (PBE,[32,50] BLYP,[50,51] BP86,[50,52–54] B97-D,[55] OLYP,[51,56] M06-L[57]), hybrid GGAs (PBE0,[32,33] B3LYP,[50,52,53,58] B3LYP*,[59] M06[60] and M06-2X[60]), a meta-GGA (TPSS[32,50,61]), a hybrid meta-GGA (TPSSh[32,50,61,62]) and a double-hybrid (B2-PLYP[63]). We employed the def2-QZVPP basis set for Mn and def2-TZVPP for all other atoms, as well as dispersion corrections according to the DFT-D3 approach.[64] These calculations were performed using TURBOMOLE v6.4[35] and GAUSSIAN 09,[65] depending on the availability of functionals.

Results and Discussion

Spin State Energetics

Results from multiconfigurational perturbation theory

The relative (adiabatic) energies obtained from CASPT2 and RASPT2 for the different electromeric states of $MnO(P)^+$ and $MnO(PF_4)^+$ are shown in Table 2. Both methods predict a closed-shell Mn^V $^1A_1$ ground state for both compounds, in accordance with the

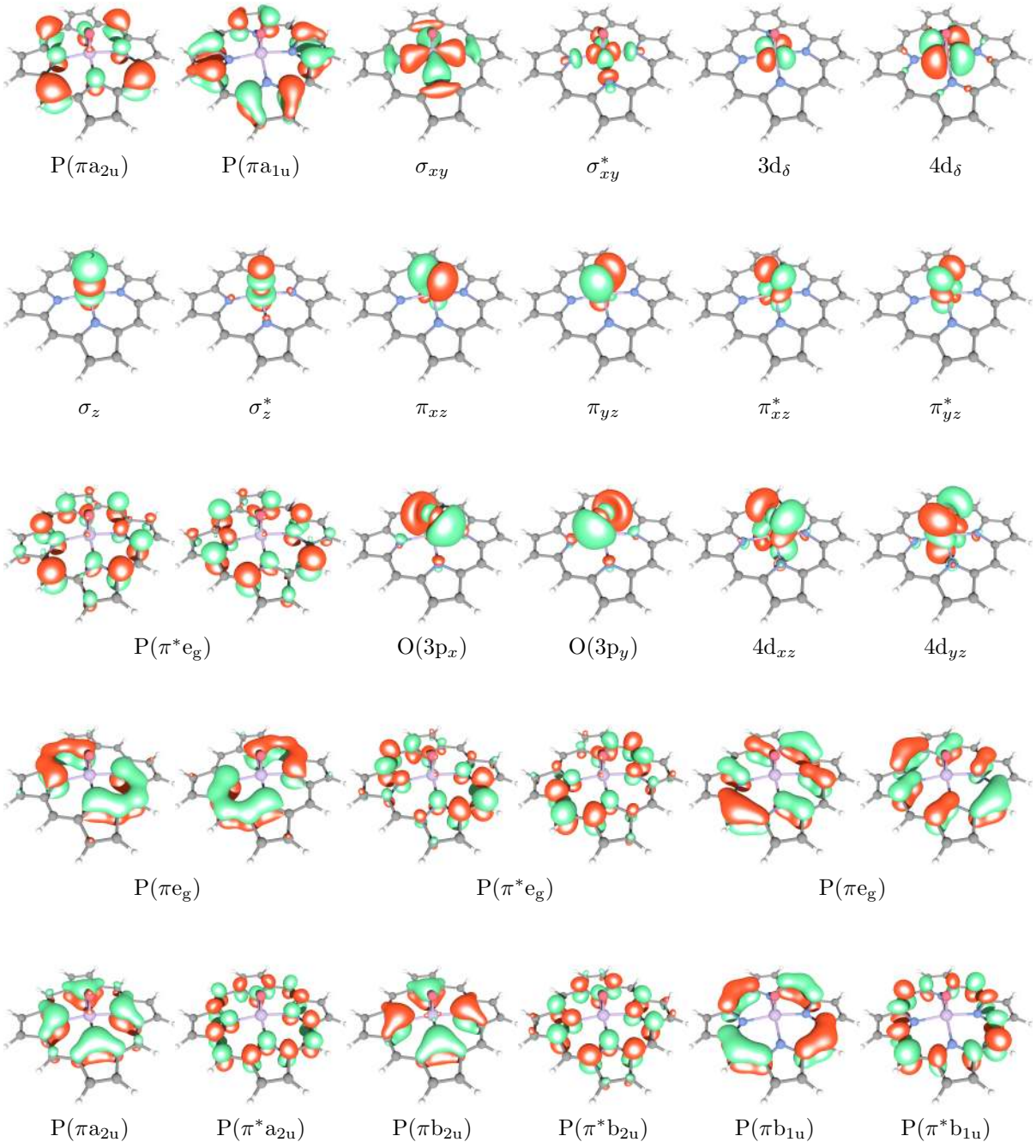

Figure 2: Plot of active orbitals at ±0.04 e a.u.$^{-3}$ contour values.

experimentally observed diamagnetic character of manganese oxo porphyrins with different substituents.[11–13] The short Mn–O bond of this state, lacking oxyl character, prevents catalytic activity in OAT reactions. Therefore, reactivity has to rely instead on the presence

of low-lying states with higher spin multiplicity, containing one or more electrons in the antibonding Mn–O π^*_{xz},π^*_{yz} orbitals.[12,17] One possibility is the Mn^V $^3B_1$ state, which is calculated at 3.9–5.6 kcal mol^{-1} above the ground state. Another possibility might be a low-lying Mn^{IV} state containing a hole in one of the HOMO, porphyrin π orbitals of either a_{1u} or a_{2u} type. As Table 2 shows, the lowest Mn^{IV} state is always a quintet state, $^5A_1$ or $^5A_2$, containing two single Mn–O π^* electrons, originating from a porphyrin π and the Mn $3d_\delta$ orbital. These observations are in accordance with the results from previous DFT studies,[17–19,24,25] although the relative energies of the different electromeric states reported from these studies are strongly dependent on the applied functional (see also the next section).

Table 2: Relative energies in kcal mol^{-1} of the electronic states of $MnO(L)^+$ with L = P and PF_4, with respect to the Mn^V $^1A_1$ state.

			$Mn^VO(L)^+$	$Mn^{IV}O(L^\bullet\ a_{2u})^+$			$Mn^{IV}O(L^\bullet\ a_{1u})^+$		
L		medium	$^3B_1$	$^5A_2$	$^3B_1$	$^1B_1$	$^5A_1$	$^3B_1$	$^1B_1$
P	CASPT2	vacuum	3.9	13.0	15.8	14.0	20.8	22.8	21.3
		solvent	3.0	6.7	13.1	11.3	14.8	20.4	19.0
	RASPT2	vacuum	5.6	18.3	21.9	21.9	19.5	22.0	22.1
		solvent	4.5	11.7	18.9	18.9	13.3	19.5	19.6
PF_4	CASPT2	solvent	4.0	−0.9	3.8	2.1	21.1	24.9	23.4
	RASPT2	solvent	5.4	3.7	9.4	9.5	19.9	25.1	25.3

Let us then compare the results obtained from CASPT2 and RASPT2. An essential difference between both methods is that in CASPT2 only the four frontier P(π) orbitals on the porphyrin (the Gouterman set) are included in the active space, while in RASPT2 the active space is further extended to 16 porphyrin π orbitals. The relative energies of states belonging to the same group in Table 2 such as Mn^V $^3B_1$–$^1A_1$, $Mn^{IV}O(L^\bullet a_{1u})$ $^3B_1$–$^5A_1$ or $Mn^{IV}O(L^\bullet a_{2u})$ $^3B_1$–$^5A_2$, differ by 2 kcal mol^{-1} or less between both methods. The reason is that these states only differ in the electronic distribution in the metal 3d shell. Conversely, comparing states belonging to different groups reveals much more pronounced differences.

In particular, we find that the relative energies obtained from RASPT2 for Mn^{IV} states containing an a_{2u} hole are considerably higher than the corresponding CASPT2 energies, while on the other hand the energies of the a_{1u} type radical states are quite similar. For $MnO(P)^+$, RASPT2 predicts both types of porphyrin radical states to be nearly degenerate, which is to be expected, as they involve an excitation out of the two HOMOs a_{1u} or a_{2u} that are very close-lying in the metal-free porphyrin ligand. As we will see in the next section (Table 3), the near-degeneracy is also corroborated by DFT (with different functionals). Previous DFT studies on substituted metalloporphyrins have also indicated that a_{1u} or a_{2u} porphyrin radical states should remain very close in energy as long as they bear similar *meso* and beta substituents.[66–68] With CASPT2 the description of the relative energy of electromeric states with a different distribution of electrons in the porphyrin P(π) shells is unbalanced, because the number of P(π) orbitals in the active space (only four) is too limited to fully capture the relaxation effects in the porphyrin π system. This was already shown previously in CASPT2/RASPT2 studies of the spin state energetics in other metal heme systems,[26,31,49] and is discussed in detail in ref. 49 (see Fig. 3 of that paper). With 16 P(π) orbitals, RASPT2 gives a more balanced treatment, and it was also shown previously that further extending the active space to the full set of 24 P(π) orbitals does not significantly alter the results with respect to the 16 P(π) orbitals used in this work.[26,31,49]

Another observation in the comparison between CASPT2 and RASPT2 concerns the relative energy between the Mn^{IV} $^3B_1$ and $^1B_1$ states, describing either ferro- or antiferromagnetic interaction between the two unpaired electrons on the MnO group and on the porphyrin. Spin coupling occurs between two electrons residing in spatially separated and orthogonal orbitals (in C_{2v}, the MnO π^* orbitals transform as b_1, b_2, whereas the porphyrin π orbitals are in a_1, a_2) and is therefore expected to be weakly ferromagnetic. Ferromagnetic coupling is indeed found in the RASPT2 results, and also in the DFT results which will be presented in the next section (Table 3). However, the CASPT2 calculations erroneously predict antiferromagnetic coupling.

In summary, the observed differences between the CASPT2 and RASPT2 results show that it is important to include more than only the four Gouterman π orbitals in the CAS reference to obtain accurate PT2 results for the relative energies of electromeric states with a different porphyrin π electron distribution.

Solvent effects (water/acetonitrile mixture) were studied for $MnO(P)^+$. The inclusion of the solvent does not alter the ordering of the spin states, either for CASPT2 or RASPT2. The main effect of the solvent is a general stabilization all excited states, reducing the energy range spanned by the different states in Table 2. The effect is small, 1 kcal mol^{-1}, for the Mn^V $^3B_1$ state, and larger but still limited to 2–3 kcal mol^{-1} for the Mn^{IV} $^{3,1}B_1$ states. However, the quintet states show a prominent stabilization by the solvent environment, of 6–7 kcal mol^{-1} by the solvent environment.

Comparing the results for $MnO(P)^+$ and $MnO(PF_4)^+$ one can see that both CASPT2 and RASPT2 predict a strong stabilization of the $Mn^{IV}O(L^\bullet a_{2u})$ states by substitution of the *meso* hydrogens by fluorines, whereas the $Mn^{IV}O(L^\bullet a_{1u})$ states are destabilized. This may be rationalized by a mesomeric effect, i.e. delocalization of electrons in the P(π a_{2u}) orbital over F($2p_z$) leading to the stabilization of a_{2u} based radical states. Such delocalization is possible for the a_{2u} orbital, as it has a significant amplitude at the *meso* carbons, while the a_{1u} orbital is nodal at these C (see Figure 2). Importantly, the stabilization of the $Mn^{IV}O(L^\bullet a_{2u})$ states is so strong that it brings the Mn^{IV} $^5A_2$ state within thermal reach of the of the Mn^V $^1A_1$ ground state.

Importance of low-lying high-spin states for catalytic activity

In order to refine the results for those states that might be important for multistate reactivity, we decided to perform a CASPT2 scan of the potential energy surface with respect to the stretching of the Mn–O bond for the Mn^V $^1A_1$ ground state and the thermally accessible excited states, *i.e.* the Mn^V $^3B_1$ state in both compounds and the $Mn^{IV}(P^\bullet a_{2u})$ $^5A_2$ for $MnO(PF_4)^+$. Figure 3 shows the potential energy curves for both molecules. All

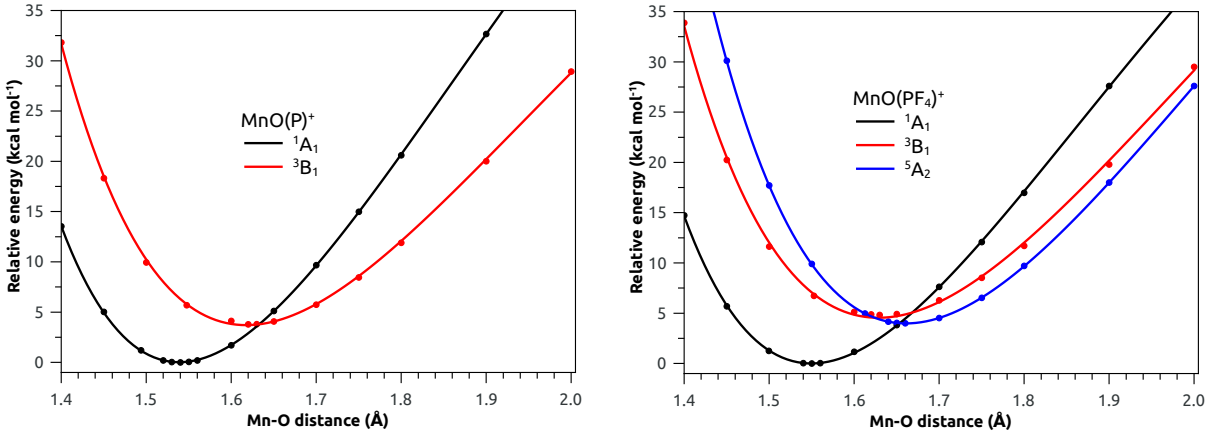

(a) (b)

Figure 3: Mn–O potential curves for $MnO(P)^+$ (a) and $MnO(PF_4)^+$ (b) obtained from CASPT2.

curves were obtained with CASPT2, including solvent effects. However, since the $^1A_1$–$^5A_2$ relative energy is not correctly described at this level, the CASPT2 curve of the $^5A_2$ state was shifted upwards by 4.6 kcal mol^{-1} (the difference between the RASPT2 and CASPT2 energies in Table 2). We believe that the shape of the $^5A_2$ curve should not be significantly different between CASPT2 and RASPT2, and the RASPT2 computations are considerably more time consuming. The CASPT2 energies were obtained using DFT structures optimized with constrained Mn–O distances. The corresponding DFT curves are presented in Figure S1. For the $^1A_1$ and $^3B_1$ state R(O)PBE0 structures were used, because the structures obtained from UPBE0 suffer from spin contamination. As can be seen from Figure S1a, the UPBE0 curve of the $^3B_1$ state is strongly different from the ROPBE0 curve, with an optimal Mn–O distance that is unrealistically long (1.68 Å) and a minimum energy which is lower than the ground state energy by 1.7 kcal mol^{-1}. For the $^1A_1$ state, both curves are the same around the Mn–O equilibrium distance, but at larger Mn–O distances (as of 1.65 Å) the UPBE0 curve deviates from RPBE0.

It should be noted that the DFT geometry optimizations were performed in vacuum, whereas the CASPT2 results in Figure 3 include solvent effects. Therefore, both sets of

potential energy curves are not strictly comparable, although according to our experience the inclusion of solvent usually has a minimal impact on molecular geometries.[69] Both with PBE0 and CASPT2, the Mn–O optimal distances in $MnO(P)^+$ and $MnO(PF_4)^+$ are close, probing a weak effect of the fluorine *meso* substituents on the bonding between the metal and the oxo ligand. The distances obtained from CASPT2 are: 1.54 Å for $^1A_1$ and 1.62 Å for the $^3B_1$ state in $MnO(P)^+$, 1.55 Å for $^1A_1$, 1.63 Å for $^3B_1$, and 1.66 Å for the $^5A_2$ state in $MnO(PF_4)^+$, reflecting progressive metal-oxo bond weakening by the presence of either zero, one, or two electrons in the Mn–O π^* MOs. The CASPT2 distances are systematically longer by 0.05–0.07 Å than the corresponding PBE0 distances (1.50 Å for $^1A_1$, 1.55 Å for $^3B_1$ (ROPBE0), 1.61 Å for $^5A_2$). However, note that the CASPT2 distance for the $^3B_1$ state remains well below the UPBE0 value (1.68 Å). The CASPT2 distance of the $^1A_1$ ground state is in close agreement with the recently reported experimental Mn–O distance of 1.546 Å in monocrystals of Mn-oxo corrolazine, showing a similar electronic structure with a Mn^V $^1A_1$ ground state.[31,70]

In energetic terms, the re-optimization of the Mn–O bond distance at the CASPT2 level does not significantly affect the adiabatic relative energies between the $^1A_1$ ground state and the triplet and quintet states: the energy differences between the minima in Figure 3 differ by less than 1 kcal mol^{-1} with the data in Table 2. Importantly, the curves in Figure 3 confirm that the reactive $^3B_1$ state is thermally accessible in both molecules, and that in $MnO(PF_4)^+$ the Mn^{IV} $^5A_2$ state is more easily reached than the $^3B_1$ state. The extent of Mn–O bond stretching needed to reach these high-spin states is limited: <0.1 Å, and the energy barriers to cross from one curve to the next are also low: < 4 kcal mol^{-1}. These data confirm the possibility of multi-state reactivity involving low-lying triplet and quintet states for OAT reactions with high-valent Mn-oxo complexes, as already suggested in previous DFT studies.[17–19,24] Nonetheless, a second requirement to achieve reactivity through high-spin states is that the oxyl character of the Mn–O bond should be significantly enhanced in these states as compared to the kinetically stable Mn^V $^1A_1$ ground state. This will be

further discussed below.

In the introduction we already mentioned a comparative study of the reactivity of $MnOP(H_2O)^+$ and MnOP(OH) for C–H bond activation, where the higher reactivity of the former complex was rationalized by a reduced energy gap between the Mn^V ground state and low-lying triplet and quintet states. Here, we find that introducing conjugated substituents at the porphyrin *meso* positions may create a similar effect. Indeed, the RASPT2 results indicate that, while the Mn^V $^3B_1$ state has a low enough energy to play a possible role in multi-state reactivity for both compounds, conjugated substituents at the *meso*-carbons can stabilize the Mn^{IV} $^5A_2$ state to such an extent that it becomes thermally accessible as well. A similar effect was also observed in a study on manganese porphyrins $Mn^{III}P^+$, where it was found that substituting *meso*-H by alkyne groups considerably lowers the energy of $P\pi \rightarrow$Mn electron transfer.[71] While this might suggest to apply conjugated substituents to improve the performance of manganese oxo-porphyrins in OAT reactions, it should be mentioned that this is not a straightforward procedure as some conjugated substituents, such as alkynes, might not be compatible with the oxidizing conditions of the reactive medium. They can be subject to an electrophilic attack by the oxo group of another catalyst, leading to their destruction.

As another example of how the equatorial ligand environment may affect multi-state reactivity of high-valent manganese oxo complexes through variation of the spin state energetics, we also want to mention here Mn-oxo corroles, *i.e.* similar complexes but with a different tetrapyrrolic macrocycle ligand. Mn^V-oxo corroles are in general stable in ambient conditions allowing easy characterization of the d^2 singlet ground state,[72,73] whereas Mn^V-oxo porphyrins are very reactive[11,74] and only stable with specific substituents[12] or in alkaline medium.[15,19] Thus, for example, the rate constant of *cis*-stilbene and *cis*-cyclooctene epoxidation by high valent manganese oxo systems is five orders of magnitude higher with *meso*-tetrakis(pentafluorophenyl)porphyrin than with *meso*-tris(pentafluorophenyl)corrole.[74] In a previous DFT study on the reactivity of Mn-oxo corroles it was concluded that a spin-transition from an kinetically stable ground state is needed to activate the OAT reaction,

Table 3: Energies in kcal mol^{-1} of $MnO(P)^+$ relative to Mn^V $^1A_1$ state calculated on top of structures optimized by PBE0/def2-TZVP.

	$Mn^VO(P)^+$	$Mn^{IV}O(P^\bullet\ a_{2u})^+$			$Mn^{IV}O(P^\bullet\ a_{1u})^+$			
	$^3B_1$	$^5A_2$	$^3B_1$	$^1B_1$	$^5A_1$	$^3B_1$	$^1B_1$	Type[a]
RASPT2	5.6	18.3	21.9	21.9	19.5	22.0	22.1	
PBE	11.1	22.7	20.7	21.1	22.0	[b]	18.1	GGA
TPSS	10.6	19.9	17.8	18.0	19.0	[b]	16.4	Meta GGA
BP86	11.2	22.3	20.3	20.6	21.4	[b]	17.9	GGA
OLYP	8.9	17.8	19.9	20.2	16.8	[b]	17.0	GGA
BLYP	10.8	20.3	17.7	18.0	19.1	[b]	15.9	GGA
M06-L	2.3	6.3	14.5	14.6	4.8	[b]	12.7	GGA
B97-D	8.0	14.2	17.4	17.6	12.9	[b]	15.6	GGA
TPSSh	7.6	12.0	12.8	12.9	10.1	10.2	10.5	Meta Hyb. 10%
B3LYP*	8.3	10.5	10.5	10.6	8.1	7.5	7.8	Hyb. 15%
B3LYP	5.6	3.5	6.4	6.5	0.8	3.0	3.2	Hyb. 20%
PBE0	1.8	0.2	5.6	5.7	−2.6	2.2	2.4	Hyb. 25%
RO-PBE0	8.6	7.6	9.5		4.6	5.8		Hyb. 25%
M06	1.3	−0.1	9.7	9.8	−4.2	5.0	5.3	Hyb. 27%
M06-2X	−10.1	−21.9	−10.5	−10.6	−26.6	−15.9	−15.6	Hyb. 54%
B2-PLYP[d]	−25.8	−39.8	−27.4	−27.8	−46.8	−35.5	[c]	Hyb. 53%
B2-PLYP[e]	50.6	55.2	60.0	60.3	53.4	57.6	[c]	Hyb. 53%

[a] Percentage indicate amount of Hartree-Fock exchange energy admixed. [b] Calculation converged to Mn^V $^3B_1$. [c] Calculation converged to $[Mn^{IV}O^\bullet(P)]^+$ instead of $[Mn^{IV}O(P^\bullet)]^+$. [d] SCF energy only. [e] SCF energy plus 27% of correlation energy calculated by MP2.

similar to Mn-oxo porphyrins.[75] From a comparison of the results obtained here for $MnO(P)^+$ with a previous C(R)ASPT2 study on the excited state energetics of Mn oxo corrole[31] we find that both the lowest excited triplet and quintet state are lower in energy, by 3–5 kcal mol^{-1}, in the case of porphyrin than for the corrole system. This strongly suggest that reactivity differences between these two systems with a very similar electronic structure may be explained by differences in their spin state energetics.

Performance of DFT functionals for excited state energetics

RASPT2 calculations of the size presented in this work are only feasible for small symmetric models, and the results may not directly be comparable to the larger metalloporphyrins investigated experimentally. For this reason, it is useful to use these RASPT2 results for benchmarking DFT functionals in order to find the optimal functional to be used in reactivity studies on more realistic systems. Energies relative to the Mn^{V} $^{1}A_{1}$ ground state of $MnO(P)^{+}$ in vacuum calculated by a series of DFT functionals are shown in Table 3. The DFT results were obtained from single-point calculations on PBE0 structures, *i.e.* the same structures as used for the C(R)ASPT2 calculations presented in Table 2. The RASPT2 results of $MnO(P)^{+}$ are presented again in Table 3 as a reference.

We first consider the relative spin state energetics for states belonging to the same metal oxidation state and with the same porphyrin P(π) occupation, that is Mn^{V} $^{3}B_{1}$ versus $^{1}A_{1}$, $Mn^{IV}(P^{\bullet}a_{2u})$ $^{3}B_{1}$ versus $^{5}A_{2}$, and $Mn^{IV}(P^{\bullet}a_{1u})$ $^{3}B_{1}$ versus $^{5}A_{1}$. As can be seen from Figure 1 all three relative energies in fact correspond to the same $3d_{\delta}\rightarrow\pi^{*}$ transition. The transition energies obtained from RASPT2 are 5.6 kcal mol^{-1} for Mn^{V} ($^{3}B_{1}$–$^{1}A_{1}$), 3.6 kcal mol^{-1} for $Mn^{IV}(P^{\bullet}a_{2u})$ ($^{3}B_{1}$–$^{5}A_{2}$), and 2.5 kcal mol^{-1} for $Mn^{IV}(P^{\bullet}a_{1u})$ ($^{3}B_{1}$–$^{5}A_{1}$). The DFT results show the expected functional dependence, observed in many previous studies on the spin state energetics in transition metal complexes:[23,76–80] GGAs almost invariably overstabilize low-spin with respect to high-spin states. This is remedied in the hybrid functionals by introducing Hartree-Fock (HF) exact exchange, but the amount of HF exchange then becomes a determinant factor for the spin state energetics: the higher the contribution of HF exchange, the more the high spin states become stabilized with respect to states with a lower spin. The result obtained from the double hybrid functional B2-PLYP needs special attention. Without MP2 correction, the results with this functional follow the trend in the hybrid functionals: with 53% HF exchange, high-spin states are strongly overstabilized. This is reversed after including 27% MP2 correlation energy, but not with complete success. The resulting $Mn^{IV}(P^{\bullet}a_{2u})$ ($^{3}B_{1}$–$^{5}A_{2}$) and $Mn^{IV}(P^{\bullet}a_{1u})$ ($^{3}B_{1}$–$^{5}A_{1}$) splittings are 4.8

and 4.2 kcal/mol respectively, close to the corresponding RASPT2 values. However, the final Mn^V ($^3B_1$–$^1A_1$) energy difference obtained from B2-PLYP, 50.6 kcal/mol, differs by as much as 44 kcal/mol from RASPT2, and is also considerably higher than the result obtained with any other functional.

Out of all functionals studied, the RASPT2 relative energies between thoses states with a common charge distribution over the metal and the porphyrin are most closely reproduced by B3LYP, with transition energies deviating by less than 1 kcal mol^{-1} between both methods for all three transitions. Among the GGAs, the best results are obtained with B97-D, closely reproducing RASPT2 for the two Mn^{IV} relative energies, while deviating by only 2.4 kcal mol^{-1} for the Mn^V ($^3B_1$–$^1A_1$) relative energy. OLYP and TPSSh also behave significantly better than the other GGAs. Also noteworthy is M06-L, which overstabilizes the high-spin states, as opposed to all other GGAs.

Second, we focus on the relative energies of Mn^{IV} and Mn^V states, by considering the data in Table 3 for the Mn^{IV} $^1B_1$ – Mn^V $^1A_1$ relative energies. With exception of (MP2 corrected) B2-PLYP, all functionals place the $^1B_1$ states at lower energy than RASPT2. Here, the GGA functionals obviously perform better than the hybrid functionals. The latter functionals show huge discrepancies with RASPT2, between 9 kcal mol^{-1} (TPSSh) and up to 50 kcal mol^{-1} (B2-PLYP, SCF result). The latter functional completely fails in describing the P→Mn charge-transfer energy, also with MP2 correction, which hugely overshoots and moves the Mn^{IV} states to unrealistically high energies. The fluctuations between the energies obtained with different GGAs are quite limited, 3.5 kcal mol^{-1} at most, with exception of M06-L predicting significantly lower energies than all other GGAs. As a note we mention that a similar behavior of different functionals was already observed previously when comparing the relative energies of Fe^{IV} and Fe^V states in FeOPCl, a model for Compound I.[26]

Two additional important points should be noted with respect to the DFT data in Table 3, (i) all DFT calculations were performed with UDFT, but in all cases the $^1A_1$ ground state was found to be pure (S=0) closed shell. For all open-shell states, the respective RODFT solutions

would be higher in energy than the UDFT values presented herein. This is illustrated by the ROPBE0 results included in Table 3, which are higher by 3.6–7.4 kcal mol^{-1} than the corresponding UPBE0 results. The difference between UDFT and RODFT is expected to be more important for the hybrid functional than for the GGAs, because spin contamination is more severe for the hybrid functionals (Table S2). (ii) With respect to the results obtained for the Mn^{V} ($^{3}B_1$–$^{1}A_1$) relative energy, it is important to note that the $^{3}B_1$ energy was obtained in all cases using the ROPBE0 structure. Using instead the optimized UPBE0 structure would have given a negative value of –1.7 kcal mol^{-1} for PBE0 (Figure S1a). Similar effects may be expected for the other hybrid functionals, showing strong diradical character and corresponding spin contamination in the UDFT solution of the $^{3}B_1$ state, leading to a weakening of the Mn-O bond. Again, these effects are much smaller for the GGA functionals.

Oxyl radical character in the ground state and low-lying excited states

The oxidative power of high-valent manganese oxo systems (both synthetic and biological, *e.g.* photosystem II) has been extensively investigated already in previous DFT studies. From all these investigations (involving water oxidation, C-H hydroxylation, etc) a crucial factor for oxidative power is the oxygen radical character in the Mn-O bond.[17,18,24,81–83] The same is true for synthetic Ru^{V}-oxo complexes, which are capable of oxidizing water. Experiments with electron paramagnetic resonance (EPR) on an ^{17}O-labeled form of a highly oxidized, short-lived Ru^{V}O intermediate have indicated a high unpaired electron density on oxygen, held responsible for its high reactivity.[84] However, it has also been shown that the strongly varying picture of the spin density distribution in the Mn-O bond given by different DFT functionals, either hybrid or GGA, is responsible for a completely different qualitative mechanistic picture of the oxidation reaction.[24]

In this section we will present an analysis of our CASSCF results with respect to oxyl

character for the low-lying states of $MnO(P)^+$ and $MnO(PF_4)^+$ that might play an important role in oxidation processes, and compare the results to the analysis of the spin density obtained from the different DFT functionals included in the benchmarking of relative spin state energetics. Oxygen radical (or oxyl) character is associated with unpaired electron(s) on the Mn-O oxygen atom. As can be seen from Figure 2 all six σ, π bonding and antibonding orbitals constituting the Mn-O bond are to some extent delocalized over the metal and oxide. Given that the bonding orbitals are fully occupied in all states, unpaired electrons on the oxide may arise from two distinctly different electronic structure features:

(a) If one (or both) of the Mn-O π^* orbitals carries an unpaired electron, this may give rise to a certain amount of oxyl character, depending on the composition of this π^* orbital. In an ionic ligand field scheme the bonding π orbital would be entirely oxygen and the antibonding π^* orbital entirely metal based, giving one unpaired electron in the metal 3d shell. In reality, however, covalent 3d–2p mixing delocalizes the unpaired electron density over the Mn-O bond, giving rise to a *positive* oxygen spin density between zero and one units.

(b) In case of an empty Mn-O π^* (or σ^*) orbital, the $\pi^2\pi^{*0}$ configuration may at first glance be expected to give zero spin density. However, when using a variational method allowing for spin polarization, such as UDFT or C(R)ASSCF (but not RDFT), the two electrons in this π bond can be redistributed by accumulating α spin density on the metal and β spin density on the oxygen. Note that in UDFT such spin redistribution is only possible at the expense of spin contamination, whereas in CASSCF the total spin is (correctly) conserved. Spin polarization introduces (partial) diradical character in the Mn-O bond, and gives a *negative* oxygen spin density between zero and one units.

Of the three states that might possibly be involved in (multi-state) reactivity in oxidative processes, the $^1A_1$ ground state does not contain any electrons in the antibonding Mn–O orbitals. UDFT calculations on this state invariably converged to a pure (S=0) state (at

the equilibrium geometry; diradical character does appear at longer Mn–O distances, see Figure S1a), as, of course, does the CASSCF wave function. With zero spin density at all points in space, oxyl character is absent in the ground state, explaining its high inertness for OAT and the need of transition to low-lying states with higher spin multiplicity, in order to explain the catalytic reactivity of the species under study. Figure 4 shows a plot of the spin density obtained from CASSCF for the Mn^{V} $^{3}B_1$ and Mn^{IV} $^{5}A_2$ states of $MnO(PF_4)^+$. With two α electrons in the π^* shell, the $^{5}A_2$ state shows a positive spin density in the Mn-O π region, while the σ bond shows a small negative region around O, indicating some diradical character in the σ bond. The (Mulliken) spin populations on oxygen are 0.30 for both the O p_x and O p_y orbitals, whereas O p_z has a small negative spin population: -0.10. On the other hand, in the $^{3}B_1$ state the π^*_{yz} is singly occupied, while π^*_{xz} and σ^*_z remain empty. Consequently, the spin density plot shows a positive π lobe along the Mn–O bond with a perpendicular negative lobe on O. The corresponding oxygen spin populations are -0.16 for O p_x, 0.26 for O p_y and -0.08 for O p_z. These numbers indicate that the oxygen gets a small but distinct oxyl character in both states. With two unpaired electrons, the $^{5}A_2$ state might be expected to be more reactive. However, the occurrence of radical character with opposite signs in O p_x, p_y in the $^{3}B_1$ state is intriguing, because it might lead to (possibly competing) reactivity along two different reaction channels.

In Figure 5 we show a comparative overview of the spin populations obtained for $MnO(P)^+$ with different functionals, making use of an (x,y)-plot where the x-axis gives the spin pop-

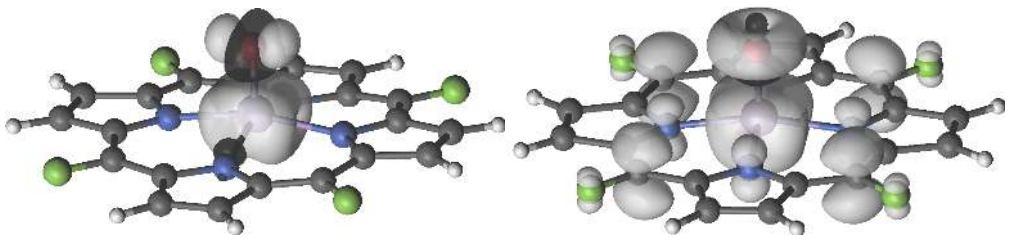

(a) (b)

Figure 4: Spin density distributions in the Mn^{V} $^{3}B_1$ state (a) and the Mn^{IV} $^{5}A_2$ state (b) of $MnO(PF_4)^+$, obtained from CASSCF.

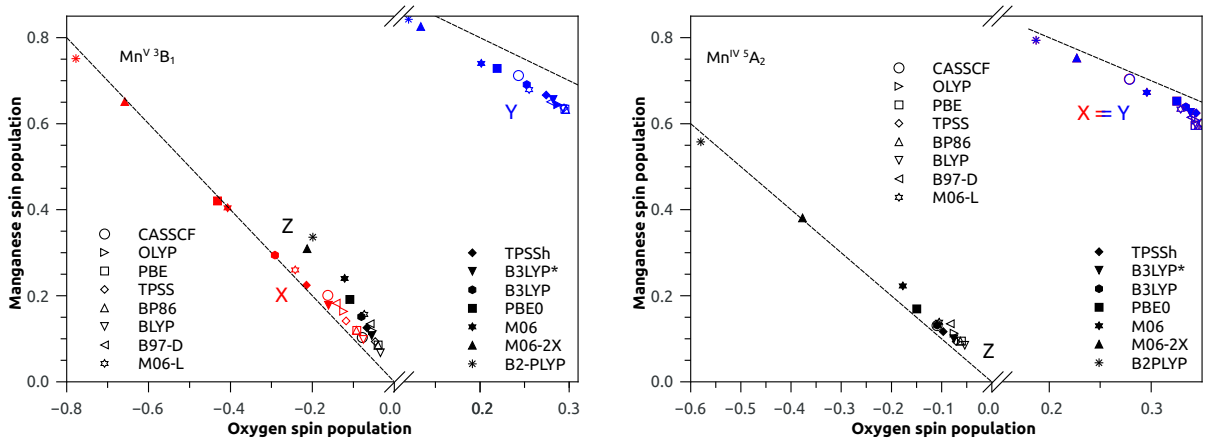

(a) (b)

Figure 5: Mulliken spin populations of Mn^V $^3B_1$ (a) and Mn^{IV} $^5A_2$ (b) divided in cartesian atomic orbitals of $MnO(P)^+$. The bonding directions X, Y and Z are identified by colors, functionals by the shape of symbols with hybrid GGA filled and pure GGA open symbols.

ulations on O p_x, p_y, and p_z and the y-axis gives the spin populations in the Mn d_{xz}, d_{yz} and d_{z^2} orbitals. The numbers obtained from CASSCF are also included and will serve as a reference. The numbers obtained from CASSCF for $MnO(P)^+$ (O p_x: -0.16, O p_y: 0.25, O p_z: -0.08 for $^3B_1$, O $p_{x,y}$:0.29, O p_z: -0.10 for $^5A_2$) are not distinctly different from the corresponding values for $MnO(PF_4)^+$, given above. This indicates that substitution effects on the reactivity of the Mn-oxo are of purely energetic nature: they affect the energy needed to reach the lowest Mn^{IV} states, but do not significantly influence the electronic distribution in the Mn–O bond. The O and Mn spin populations should add up to (approximately) one for the π_{xz} and π_{yz} bonds in the $^5A_2$ state, as well as for the π_{yz} bond in the $^3B_1$ state. The other bonds should give numbers that add up to (approximately) zero. Dashed lines corresponding to $x + y = 1$ and $x + y = 0$ are shown in the plots as a guide to the eyes.

For π bonds carrying an unpaired electron the spin populations in Figure 5 reflect the composition of the π^* orbital. As is the case with CASSCF and conform with the ligand field picture, all DFT functionals predict the π^* orbitals to be predominantly metal based: the maximum spin population on O remains < 0.3, and > 0.7 for Mn. A larger O spin population reflects a more covalent Mn–O π bond. As one can see, all GGAs predict a higher

covalency than CASSCF, and the results with different GGAs are very close. Amongst the hybrid functionals, the covalency of the bond decreases as the contribution of HF exchange increases. In fact, very limited oxyl radical character in these π bonds is predicted by functionals containing more than 50% exact exchange: B2-PLYP and M06-2X. These results are consistent with the fact that the Hartree-Fock method gives too ionic metal-ligand bonds, while pure DFT functionals predict more covalent metal-ligand bonds.

Looking next at the σ bond, small negative O spin populations point to a small contribution of diradical character. This is what would be expected for a (strong) σ bond, and what is found with CASSCF and with most functionals. All GGAs predict less than 10% diradical character for the σ bond, (slightly) less than with CASSCF. Hybrid functionals are known to give a higher diradical character (and corresponding spin contamination) than pure functionals, and the more so as the HF contribution increases.[85] This behaviour is corroborated by the spin populations in Figure 5. With 'traditional' functionals B3LYP, PBE0, TPSSh the diradical character of the σ bond still remains below 20%. However, excessively high oxygen spin populations are predicted by M06-2X and B2-PLYP. With the latter functional, the Mn–O σ bond in the Mn^{IV} $^5A_2$ state is predicted to contain a higher than 50% diradical contribution!

A similar, but more pronounced effect is found for the π_{xz} bond in the Mn^{V} $^3B_1$ state, with π^*_{xz} empty. Here we find oxygen spin populations ranging between -0.07 and -0.78 over the range of considered DFT functionals, which therefore predict a diradical contribution to this π bond ranging between only 7% and as much as 78%. With exception of M06-L, all GGAs predict oxygen spin populations that are smaller (in absolute value) than with CASSCF, and the difference between the functionals is rather small, ranging between -0.07 with BLYP to -0.14 with B97-D (as compared to -0.16 with CASSCF). The hybrid functionals with lowest HF exchange (B3LYP*, 15% and TPSSh, 10%) give -0.16 and -0.21 respectively, but this increases progressively to -0.78 with B2-PLYP, containing 53% HF exchange.

It is important to note that the plots in Figure 5 were generated using DFT data obtained

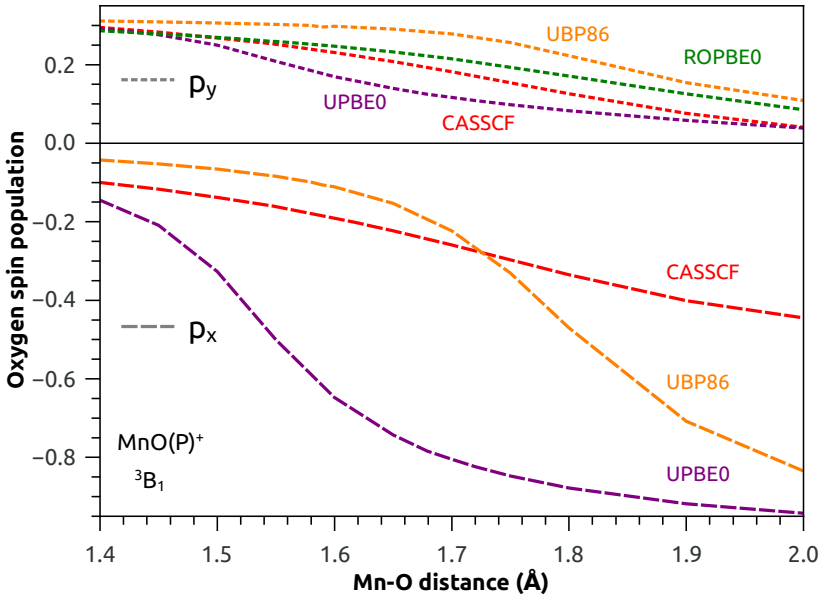

Figure 6: Oxygen Mulliken spin population in p_x and p_y orbitals as a function of Mn–O distance.

at structures optimized with PBE0. For the $^3B_1$ state, ROPBE0 structures were used (Mn–O distance = 1.55 Å) to avoid the unrealistically long Mn–O distance (1.68 Å) predicted by UPBE0 (*cf.* Figure S1a). But enhancing the diradical character (at the expense of increasing spin contamination) is precisely the driving force leading to a (much) longer Mn–O equilibrium distances in UDFT versus RDFT calculations, when making use of hybrid functionals. As such, the O p_x spin populations in Figure 5 should become even more negative if they would instead be obtained at Mn–O distances that are optimized at the UDFT level (with the respective hybrid functionals). This is illustrated in Figure 6, showing the O p_x and p_y spin populations of the $^3B_1$ state as a function of the Mn–O distance, calculated with ROPBE0, UPBE0, UBP86 and CASSCF. Each calculation used to construct these plots was performed at its own optimized geometry (at fixed Mn–O distances). The corresponding DFT energy profiles are shown in Figure S1, the CASSCF data were obtained with ROPBE0 structures (*cf.* Figure 3).

At $R_{\text{Mn-O}} = 1.55$ Å, corresponding to the ROPBE0 minimum, the O p_x spin populations

are close to the values shown in Figure 5: −0.50 for UPBE0, −0.08 for UBP86, −0.16 for CASSCF while the diradical character of the π_{xz} bond is (by definition) zero with ROPBE0. The UPBE0 O p_x spin population falls down steeply with the Mn–O distance. At the UPBE0 minimum ($R_{\text{Mn-O}} = 1.68$ Å), it reaches a value of −0.78. As such, UPBE0 predicts a very pronounced oxyl character for the $^3B_1$ state, corresponding to a *negative* oxygen spin population. On the other hand, as illustrated by the BP86 results, pure GGAs are much more resistant to spin contamination.[85] The Mn–O distance obtained from UBP86, 1.59 Å, remains much closer to the ROPBE0 minimum, and the O p_x spin population is much more reluctant to fall down, starting its descent only at distances > 1.7 Å. The O p_x populations obtained from CASSCF rather predict a steady increase of negative O p_x spin density and concomitant diradical character with the Mn–O distance.

It is also worthwhile to look at the O p_y populations in Figure 6. The absolute values obtained with different methods are different - reflecting the covalency of the π_{yz} bond (see above). However, they all show the same decreasing behavior with the Mn–O distance, indicating that as the Mn–O bond dissociates the unpaired electron in this π bond will localize on Mn $3d_{yz}$, leaving O p_y fully occupied. A similar plot obtained for the $^5A_2$ state (Figure S2) shows the same trend, with both unpaired electrons moving towards the Mn 3d shell as the Mn–O bond dissociates.

Armed with these observations it becomes quite straightforward to rationalize the different reactivity patterns observed for the Mn^V $^3B_1$ state in Mn-oxo porphyrins from previous DFT studies, either with pure or hybrid functionals.[17–19,24] With pure GGAs, limited diradical (negative O p_x spin density) is predicted for the π_{xz} bond in the $^3B_1$ state, whereas the bonds carrying an unpaired electron (π_{yz} in the $^3B_1$ state and both π orbitals in low-lying quintet Mn^{IV} states) contain significant oxyl character (positive O $p_{y,(x)}$ spin density). The resulting *positive* spin population on oxygen (see also Figure S3) is invoked to rationalize reactivity for C–H abstraction in the $^3B_1$ excited states. On the other hand, with hybrid functionals, the singly occupied π^*_{yz} orbital is much more localized on the metal, giving a

much smaller (positive) O p_y spin population, whereas the diradical character of the π_{xz} bond is much more pronounced. Thus, with hybrid functionals Mn–O oxyl character and corresponding reactivity is instead connected to the *negative* O spin population. Both 'types' of triplet states are denoted as resp. $^3\Pi_{xz}$ and $^3\Pi_o$ in ref. 24, and are shown in that study to lead to very different reactivity patterns and barriers heights for OAT reactions. As the CASSCF results indicate, both types of radical character are in fact united in one state. Further studies are needed to establish their relative importance for reactivity.

Conclusions

In this work, porphyrin complexes with an manganese-oxo group, $MnO(P)^+$ and $MnO(PF_4)^+$, were studied by means of second-order perturbation theory based on either Complete Active Space (CASPT2) and Restricted Active Space (RASPT2) wave functions. These complexes serve as a model to investigate two important electronic structure aspects of manganese-oxo heme systems that play a determinant role for their catalytic reactivity in OAT reactions, that is (a) spin state energetics, and (b) oxyl radical character of the manganese-oxo bond.

All possible low-lying Mn^V states and Mn^{IV} states with a porphyrin radical of either a_{1u} or a_{2u} type were considered. Conform with experiment, the ground state of both molecules is a Mn^V singlet ($^1A_1$). A triplet state ($^3B_1$) corresponding to the excitation of an electron from the non-bonding $3d_\delta$ orbital to one of the Mn–O π^* orbitals is found to be thermally accessible in both complexes. The Mn^{IV} states are high-lying in $MnO(P)^+$, but substitution of hydrogen by fluorine at the *meso* positions of the macrocyle causes a stabilization of Mn^{IV} states with a $P(\pi a_{2u})$ radical, placing the Mn^{IV} $^5A_2$ state below the Mn^V $^3B_1$ state. Similar to our previous findings[26,31] the RASPT2 calculations (with an active space containing 16 porphyrin π^* orbitals) are superior to CASPT2, because the active space in the latter method is too small to accurately describe (a) the splitting between a_{2u} and a_{1u} type radicals on the porphyrin and (b) spin interaction between Mn^{IV} and the porphyrin radical. Including

solvent effects in the calculations is essential to obtain an accurate picture of the excited state energetics, as it significantly stabilizes Mn^{IV} with respect to Mn^{V} states.

Oxyl radical character in the $^3B_1$ and $^5A_2$ states are investigated by analyzing the CASSCF spin density distribution along the Mn–O bond in terms of the three contributions: σ (Mn d_{z^2}–O p_z), π_{xz} (Mn d_{xz}–O p_x), π_{yz} (Mn d_{yz}–O p_y). Two sources of oxyl radical character emerge from this analysis: (a) a positive oxygen spin density resulting from the occupation of π^* orbitals, and (b) a negative oxygen spin density resulting from diradical contributions to the CASSCF wave function for those bonds where the antibonding component is empty. The σ bond shows a very limited diradical contribution. However, for the $^3B_1$ state we find a remarkably large diradical character in the π_{xz} bond, which grows steadily as the Mn–O bond is stretched. Further studies are necessary to establish which of the two radical types plays a dominant role in OAT reactivity.

Both aspects, spin state energetics and oxyl radical character, were also studies with an extensive range of DFT functionals. As usual, hybrid functionals (B3LYP in particular) were found to outperform GGAs in predicting the spin promotion energy between states differing only in the distribution of electrons in the Mn 3d shell. The latter functionals are, however, clearly superior in describing the relative position of Mn^{IV} with respect to Mn^{V} states. On the whole, the functional that comes closest to RASPT2 in describing the relative energetics is B97-D. The description of diradical character of the π_{xz} bond in the $^3B_1$ state was found to be problematic for hybrid functionals containing more than 15% HF exchange. GGAs in general seem to underestimate diradical bond contributions, but also here B97-D comes closest to the multiconfigurational wave function description. Functionals that show disappointing behavior are the Minnesota functionals, M06, M06-L and M06-2X, as well as the B2-PLYP functional. The inclusion of MP2 correlation in B2-PLYP can obviously not correct for the flaws that are introduced by giving this functional such a high amount of HF exchange.

Supporting Information Available

Relevant geometrical features, energy profile along Mn–O distance by DFT/PBE0, BP86 for $MnO(P)^+$ and $MnO(PF_4)^+$, plots of oxygen Mulliken spin population in p_x, p_y and p_z orbitals obtained by CASSCF, values of $\langle S^2 \rangle$ of UDFT calculations of Table 3, total spin population of manganese as a function of total spin population of oxygen for Mn^{V} $^3B_1$ and Mn^{IV} $^5A_2$ states of $MnO(P)^+$and fully optimized geometries. This material is available free of charge via the Internet at `http://pubs.acs.org/`.

Acknowledgement

The authors thank Prof. Jeremy Harvey for helpful discussions. The National Council of Technological and Scientific Development – CNPq (grants 402627/2012-1, 202911/2014-4 and 203083/2015-6), Flemish Science Foundation – FWO are acknowledged for the financial support. The computational resources and services used in this work were provided by the VSC (Flemish Supercomputer Center), funded by the Hercules Foundation and the Flemish Government – department EWI.

References

(1) Meunier, B.; De Visser, S. P.; Shaik, S. *Chem. Rev.* **2004**, *104*, 3947–3980.

(2) Shaik, S.; Kumar, D.; de Visser, S. P.; Altun, A.; Thiel, W. *Chem. Rev.* **2005**, *105*, 2279–2328.

(3) Lonsdale, R.; Harvey, J. N.; Mulholland, A. J. *J. Chem. Theory Comput.* **2012**, *8*, 4637–4645.

(4) Lonsdale, R.; Houghton, K. T.; Żurek, J.; Bathelt, C. M.; Foloppe, N.; de Groot, M. J.; Harvey, J. N.; Mulholland, A. J. *J. Am. Chem. Soc.* **2013**, *135*, 8001–8015.

(5) Yachandra, V. K.; Sauer, K.; Klein, M. P. *Chem. Rev.* **1996**, *96*, 2927–2950.

(6) Tabushi, I. *Coordin. Chem. Rev.* **1988**, *86*, 1–42.

(7) Meunier, B. *Chem. Rev.* **1992**, *92*, 1411–1456.

(8) Sheldon, R. A., Ed. *Metalloporphyrins in Catalytic Oxidations*; Marcel Dekkers, Inc., 1994.

(9) Woggon, W.-D. In *Bioorganic Chemistry*; Schmidtchen, F., Ed.; Topics in Current Chemistry; Springer Berlin Heidelberg, 1997; Vol. 184; pp 39–96.

(10) Zanardi, F. B.; Barbosa, I. A.; de Sousa Filho, P. C.; Zanatta, L. D.; da Silva, D. L.; Serra, O. A.; Iamamoto, Y. *Microporous Mesoporous Mater.* **2016**, *219*, 161–171.

(11) Groves, J. T.; Lee, J.; Marla, S. S. *J. Am. Chem. Soc.* **1997**, *119*, 6269–6273.

(12) Jin, N.; Groves, J. T. *J. Am. Chem. Soc.* **1999**, *121*, 2923–2924.

(13) Song, W. J.; Seo, M. S.; DeBeer George, S.; Ohta, T.; Song, R.; Kang, M.-J.; Tosha, T.; Kitagawa, T.; Solomon, E. I.; Nam, W. *J. Am. Chem. Soc.* **2007**, *129*, 1268–1277.

(14) Groves, J. T.; Watanabe, Y.; McMurry, T. J. *J. Am. Chem. Soc.* **1983**, *105*, 4489–4490.

(15) Jin, N.; Bourassa, J. L.; Tizio, S. C.; Groves, J. T. *Angew. Chem. Int. Ed.* **2000**, *39*, 3849–3851.

(16) Jin, N.; Ibrahim, M.; Spiro, T. G.; Groves, J. T. *J. Am. Chem. Soc.* **2007**, *129*, 12416–12417.

(17) Balcells, D.; Raynaud, C.; Crabtree, R. H.; Eisenstein, O. *Inorg. Chem.* **2008**, *47*, 10090–10099.

(18) Balcells, D.; Raynaud, C.; Crabtree, R. H.; Eisenstein, O. *Chem. Commun.* **2008**, 744–746.

(19) De Angelis, F.; Jin, N.; Car, R.; Groves, J. T. *Inorg. Chem.* **2006**, *45*, 4268–4276.

(20) Ghosh, A.; Persson, B. J.; Taylor, P. R. *J. Biol. Inorg. Chem.* **2003**, *8*, 507–511.

(21) Ghosh, A.; Taylor, P. R. *Current Opin. Chem. Biol.* **2003**, *7*, 113–124.

(22) Radoń, M. *J. Chem. Theory Comput.* **2014**, *10*, 2306–2321.

(23) Vancoillie, S.; Zhao, H.; Radoń, M.; Pierloot, K. *J. Chem. Theory Comput.* **2010**, *6*, 576–582.

(24) Sameera, W.; McGrady, J. E. *Dalton Trans.* **2008**, 6141–6149.

(25) de Visser, S. P.; Ogliaro, F.; Gross, Z.; Shaik, S. *Chem. Eur. J.* **2001**, *7*, 4954–4960.

(26) Radoń, M.; Broclawik, E.; Pierloot, K. *J. Chem. Theory Comput.* **2011**, *7*, 898–908.

(27) Andersson, K.; Malmqvist, P.-Å.; Roos, B. O. *J. Chem. Phys.* **1992**, *96*, 1218–1226.

(28) Malmqvist, P.-Å.; Pierloot, K.; Shahi, A. R. M.; Cramer, C. J.; Gagliardi, L. *J. Chem. Phys.* **2008**, *128*, 204109.

(29) Kepenekian, M.; Calborean, A.; Vetere, V.; Le Guennic, B.; Robert, V.; Maldivi, P. *J. Chem. Theory Comput.* **2011**, *7*, 3532–3539.

(30) Chen, H.; Lai, W.; Shaik, S. *J. Phys. Chem. B* **2011**, *115*, 1727–1742.

(31) Zhao, H.; Pierloot, K.; Langner, E. H.; Swarts, J. C.; Conradie, J.; Ghosh, A. *Inorg. Chem.* **2012**, *51*, 4002–4006.

(32) (a) Perdew, J. P.; Wang, Y. *Phys. Rev. B* **1992**, *45*, 13244; (b) Perdew, J. P.; Burke, K.; Ernzerhof, M. *Phys. Rev. Lett.* **1996**, *77*, 3865.

(33) Perdew, J. P.; Ernzerhof, M.; Burke, K. *J. Chem. Phys.* **1996**, *105*, 9982–9985.

(34) Weigend, F.; Ahlrichs, R. *Phys. Chem. Chem. Phys.* **2005**, *7*, 3297–3305.

(35) Ahlrichs, R.; Bär, M.; Häser, M.; Horn, H.; Kölmel, C. *Chem. Phys. Lett.* **1989**, *162*, 165–169.

(36) Werner, H.-J.; Knowles, P. J.; Knizia, G.; Manby, F. R.; Schütz, M. *WIRES Comput. Mol. Sci.* **2012**, *2*, 242–253.

(37) Aquilante, F.; De Vico, L.; Ferré, N.; Ghigo, G.; Malmqvist, P.-Å.; Neogrády, P.; Pedersen, T. B.; Pitoňák, M.; Reiher, M.; Roos, B. O.; Serrano-Andrés, L.; Urban, M.; Veryazov, V.; Lindh, R. *J. Comput. Chem.* **2010**, *31*, 224–247.

(38) (a) Roos, B. O.; Lindh, R.; Malmqvist, P.-Å.; Veryazov, V.; Widmark, P.-O. *J. Phys. Chem. A* **2004**, *108*, 2851–2858; (b) Roos, B. O.; Lindh, R.; Malmqvist, P.-Å.; Veryazov, V.; Widmark, P.-O. *J. Phys. Chem. A* **2005**, *109*, 6575–6579.

(39) In the beginning of 2015 an error was discovered in the ANO-rcc basis set of C, included in MOLCAS versions 6.4–8.0. The basis set was replaced by a new correct ANO-rcc basis set, which can be found at http://www.molcas.org/ANO. All CASPT2/RASPT2 calculations presented in this work were performed with the correct C basis set.

(40) Reiher, M.; Wolf, A. *J. Chem. Phys.* **2004**, *121*, 10945–10956.

(41) Aquilante, F.; Malmqvist, P.-Å.; Pedersen, T. B.; Ghosh, A.; Roos, B. O. *J. Chem. Theory Comput.* **2008**, *4*, 694–702.

(42) Cossi, M.; Rega, N.; Scalmani, G.; Barone, V. *J. Chem. Phys.* **2001**, *114*, 5691–5701.

(43) This is the experimental value of the mixture H_2O:CH_3CN in the molar ratio of 7:3,[86] which is a composition suitable to solubilize *meso*-aryl metalloporphyrins, oxygen donors such as hydrogen peroxide and *meta*-chloroperbenzoic acid and a variety of organic molecules able to undergo oxidation.

(44) Ghigo, G.; Roos, B. O.; Malmqvist, P.-Å. *Chem. Phys. Lett.* **2004**, *396*, 142–149.

(45) Forsberg, N.; Malmqvist, P.-Å. *Chem. Phys. Lett.* **1997**, *274*, 196 – 204.

(46) Pierloot, K. In *Comput. Organomet. Chem.*; Cundari, T., Ed.; Marcel Dekker, Inc.: New York, 2001; pp 123–157.

(47) Roos, B. O.; Andersson, K.; Fülscher, M. P.; Malmqvist, P.-Å.; Serrano-Andrés, L.; Pierloot, K.; Merchán, M. *Advances in Chemical Physics: New Methods in Computational Quantum Mechanics, Volume 93* **2007**, 219–331.

(48) Pierloot, K. *Mol. Phys.* **2003**, *101*, 2083–2094.

(49) Vancoillie, S.; Zhao, H.; Tran, V. T.; Hendrickx, M. F.; Pierloot, K. *J. Chem. Theory Comput.* **2011**, *7*, 3961–3977.

(50) (a) Dirac, P. A. M. *Proc. R. Soc. A* **1929**, 714–733; (b) Slater, J. C. *Phys. Rev.* **1951**, *81*, 385.

(51) Lee, C.; Yang, W.; Parr, R. G. *Phys. Rev. B* **1988**, *37*, 785–789.

(52) Vosko, S.; Wilk, L.; Nusair, M. *Can. J. Phys.* **1980**, *58*, 1200–1211.

(53) Becke, A. D. *Phys. Rev. A* **1988**, *38*, 3098.

(54) Perdew, J. P. *Phys. Rev. B* **1986**, *33*, 8822.

(55) Grimme, S. *J. Comput. Chem.* **2006**, *27*, 1787–1799.

(56) Handy, N. C.; Cohen, A. J. *Mol. Phys.* **2001**, *99*, 403–412.

(57) Zhao, Y.; Truhlar, D. G. *J. Chem. Phys.* **2006**, *125*, 194101.

(58) Becke, A. D. *J. Chem. Phys.* **1993**, *98*, 5648–5652.

(59) Reiher, M.; Salomon, O.; Hess, B. A. *Theor. Chem. Acc.* **2001**, *107*, 48–55.

(60) Zhao, Y.; Truhlar, D. G. *Theor. Chem. Acc.* **2008**, *120*, 215–241.

(61) Tao, J.; Perdew, J. P.; Staroverov, V. N.; Scuseria, G. E. *Phys. Rev. Lett.* **2003**, *91*, 146401.

(62) Staroverov, V. N.; Scuseria, G. E.; Tao, J.; Perdew, J. P. *J. Chem. Phys.* **2003**, *119*, 12129–12137.

(63) Grimme, S. *J. Chem. Phys.* **2006**, *124*, 034108.

(64) Grimme, S.; Antony, J.; Ehrlich, S.; Krieg, H. *J. Chem. Phys.* **2010**, *132*, 154104.

(65) Frisch, M. et al. Gaussian 09, Revision D. 01; Gaussian: Wallingford, CT, USA, 2009.

(66) Vangberg, T.; Lie, R.; Ghosh, A. *J. Am. Chem. Soc.* **2002**, *124*, 8122–8130.

(67) Hirao, H.; Shaik, S.; Kozlowski, P. M. *J. Phys. Chem. A* **2006**, *110*, 6091–6099.

(68) Prendergast, K.; Spiro, T. G. *J. Phys. Chem.* **1991**, *95*, 9728–9736.

(69) Formiga, A. L. B.; Vancoillie, S.; Pierloot, K. *Inorg. Chem.* **2013**, *52*, 10653–10663.

(70) Baglia, R. A.; Prokop-Prigge, K. A.; Neu, H. M.; Siegler, M. A.; Goldberg, D. P. *J. Am. Chem. Soc.* **2015**, *137*, 10874–10877.

(71) Kepenekian, M.; Vetere, V.; Le Guennic, B.; Maldivi, P.; Robert, V. *Chem. – Eur. J.* **2011**, *17*, 12045–12050.

(72) Gross, Z.; Golubkov, G.; Simkhovich, L. *Angew. Chem. Int. Ed.* **2000**, *39*, 4045–4047.

(73) Liu, H.-Y.; Mahmood, M. H.; Qiu, S.-X. S.; Chang, C. K. *Coordin. Chem. Rev.* **2013**, *257*, 1306–1333.

(74) Zhang, R.; Newcomb, M. *Acc. Chem. Res.* **2008**, *41*, 468–477.

(75) Zhu, C.; Liang, J.; Wang, B.; Zhu, J.; Cao, Z. *Phys. Chem. Chem. Phys.* **2012**, *14*, 12800–12806.

(76) Pierloot, K.; Vancoillie, S. *J. Chem. Phys.* **2006**, *125*, 124303–124303.

(77) Pierloot, K.; Vancoillie, S. *J. Chem. Phys.* **2008**, *128*, 034104.

(78) Radoń, M.; Pierloot, K. *J. Phys. Chem. A* **2008**, *112*, 11824–11832.

(79) Radoń, M.; Broclawik, E.; Pierloot, K. *J. Phys. Chem. B* **2010**, *114*, 1518–1528.

(80) Pierloot, K.; Zhao, H.; Vancoillie, S. *Inorg. Chem.* **2010**, *49*, 10316–10329.

(81) Siegbahn, P. E. M.; Crabtree, R. H. *J. Am. Chem. Soc.* **1999**, *121*, 117–127.

(82) Siegbahn, P. E. M. *Inorg. Chem.* **2000**, *39*, 2923–2935.

(83) Siegbahn, P. E. M. *Accounts Chem. Res.* **2009**, *42*, 1871–1880.

(84) Moonshiram, D.; Alperovich, I.; Concepcion, J. J.; Meyer, T. J.; Pushkar, Y. *Proc. Natl. Acad. Sci. U.S.A.* **2013**, *110*, 3765–3770.

(85) Lee, A. M.; Handy, M. C. *J. Chem. Soc., Faraday Trans.* **1993**, 3999–4003.

(86) Moreau, C.; Douhéret, G. *J. Chem. Thermodynamics* **1976**, *8*, 403–410.

For Table of Contents Only

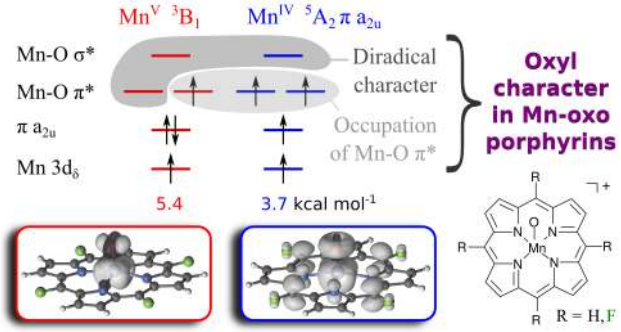

Different electromeric states in manganese-oxo porphyrins were investigated with DFT and multiconfigurational perturbation theory, focusing on their role in oxygen transfer reactivity. The ground state is Mn^{V} singlet. Possible reactive states are a Mn^{V} triplet and a $Mn^{IV}O(L^{\bullet}a_{2u})^{+}$ quintet. The latter state is strongly stabilized by substituting H by F at the *meso* carbons. Oxyl character is rationalized in terms of unpaired electrons in Mn–O π^{*} orbitals and Mn–O bond diradical character.

Supporting Information

Spin-State Energetics and Oxyl Character of Mn-Oxo Porphyrins by Multiconfigurational ab initio Calculations: Implications on Reactivity

Sergio Augusto Venturinelli Jannuzzi[a,b], Quan Manh Phung[b], Alex Domingo[b], André Luiz Barboza Formiga[a] and Kristine Pierloot[b].

[a] *Institute of Chemistry, P.O. Box 6154, University of Campinas – UNICAMP, 13083-970, Campinas, SP, Brazil.* [b] *Department of Chemistry, KU Leuven, Celestijnenlaan 200F, B-3001 Leuven, Belgium.*

Supplementary tables

- $r_{i\text{-}j}$ is the distance between atoms i and j.
- Δ is the distance between Mn atom and the average plane formed by the four nitrogens.
- τ is defined as the difference between two N–Mn–N of opposing pyrroles, divided by 60.[1] It equals 0 for square pyramid and 1 for trigonal bipyramidal, so it is a measure of how the coordination sphere of pentacoordinated metals arranges between these two extremes.
- *tilt* is the dihedral angle formed between four β carbons of opposing pyrroles.

Table S1: Relevant geometrical features of $MnO(P)^+$ and $MnO(PF_4)^+$optimized by PBE0/def2-TZVP.

State	$R_{\text{Mn-O}}$ (Å)	$R_{\text{Mn-N3}}$ (Å)	$R_{\text{Mn-N4}}$ (Å)	Δ (Å)	τ	*tilt* (°)
			P			
$Mn^{V}O(L^{2-})^+$						
$^1A_1$	1.494	1.978	1.978	0.454	0.000	23.10
$^3B_1$	1.680	1.992	1.992	0.309	0.000	15.10
$^3B_1$(ROPBE0)	1.548	2.013	1.964	0.376	0.240	0.00
$Mn^{IV}O(L^{\bullet-})^+$ π a_{1u}						
$^5A_1$	1.618	2.010	2.010	0.272	0.000	0.00
$^5A_1$(ROPBE0)	1.610	2.010	2.010	0.272	0.000	0.00
$^1B_1$	1.547	2.028	1.989	0.368	0.155	0.00
$^3B_1$	1.548	2.027	1.989	0.367	0.152	0.00
$^3B_1$(ROPBE0)	1.545	2.027	1.989	0.368	0.153	0.00
$Mn^{IV}O(L^{\bullet-})^+$ π a_{2u}						
$^5A_2$	1.614	2.023	2.023	0.257	0.000	0.00
$^5A_2$(ROPBE0)	1.606	2.022	2.022	0.261	0.000	0.00
$^1B_1$	1.543	1.999	2.043	0.351	0.138	0.00
$^3B_1$	1.543	1.999	2.043	0.352	0.142	0.00
$^3B_1$(ROPBE0)	1.542	1.998	2.042	0.354	0.143	0.00
			PF_4			
$Mn^{V}O(L^{2-})^+$						
$^1A_1$	1.50	1.98	1.98	0.46	0.00	21.10
$^3B_1$	1.55	2.02	1.97	0.39	0.22	0.00
$Mn^{IV}O(L^{\bullet-})^+$ π a_{1u}						
$^5A_1$	1.62	2.01	2.01	0.28	0.00	0.00
$^1B_1$	1.55	2.03	1.99	0.37	0.16	0.00
$^3B_1$	1.55	2.03	1.99	0.37	0.16	0.00
$Mn^{IV}O(L^{\bullet-})^+$ π a_{2u}						
$^5A_2$	1.61	2.02	2.02	0.26	0.00	0.00
$^1B_1$	1.54	2.00	2.04	0.35	0.14	0.00
$^3B_1$	1.54	2.00	2.04	0.35	0.14	0.00

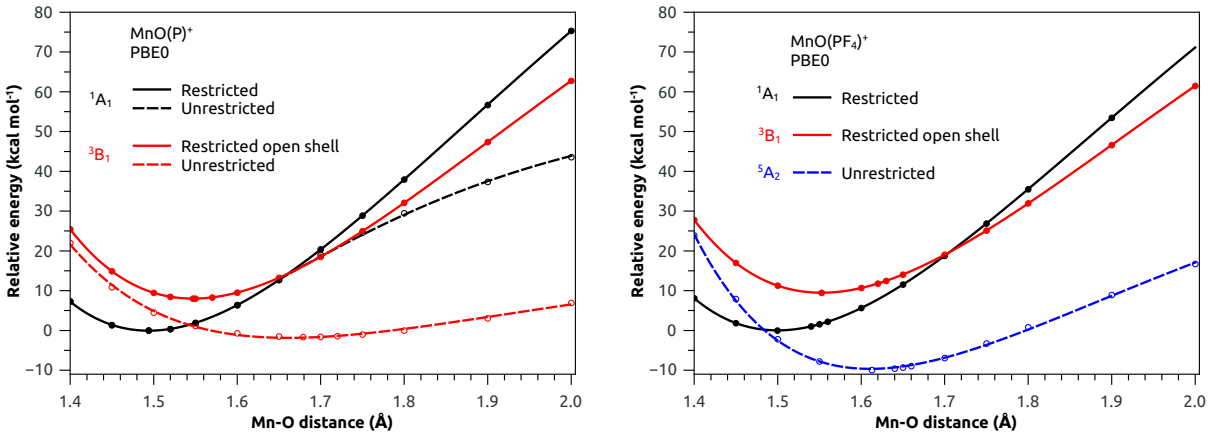

(a) (b)

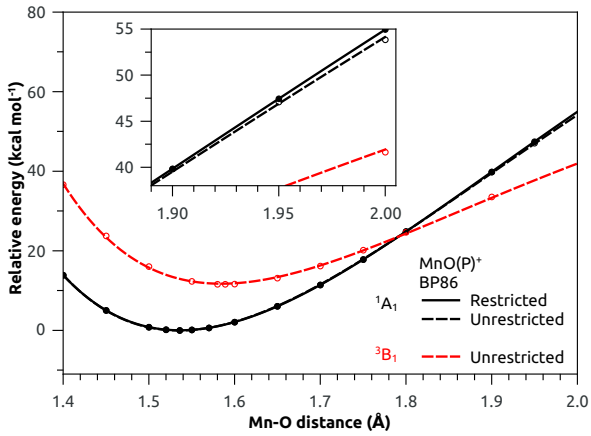

(c)

Figure S1: Mn–O potential curves for calculated by DFT/PBE0 for $MnO(P)^+$ (a) and $MnO(PF_4)^+$ (b) and by BP86 for $MnO(P)^+$ (c).

Table S2: Values of $\langle S^2 \rangle$ of DFT single point calculations on top of structures optimized by PBE0/def2-TZVP using def2-QZVPP(Mn) and def2-TZVPP(others) basis set.

	$Mn^{V}OP$		$Mn^{IV}OP^{\bullet}$ a_{2u}			$Mn^{IV}OP^{\bullet}$ a_{1u}		
Functional	$^1A_1$	$^3B_1$	$^5A_2$	$^1B_1$	$^3B_1$	$^5A_1$	$^1B_1$	$^3B_1$
PBE	0.000	2.037	6.039	1.016	2.014	6.038	1.006	[a]
TPSS	0.000	2.045	6.045	1.025	2.023	6.041	1.013	[a]
BP86	0.000	2.037	6.041	1.018	2.016	6.040	1.007	[a]
OLYP	0.000	2.071	6.054	1.019	2.016	6.055	1.007	[a]
BLYP	0.000	2.027	6.034	1.015	2.013	6.034	1.006	[a]
M06-L	0.000	2.155	6.078	1.032	2.029	6.075	1.023	[a]
B97-D	0.000	2.088	6.068	1.025	2.021	6.069	1.011	[a]
TPSSh	0.000	2.101	6.072	1.045	2.042	6.064	1.033	2.038
B3LYP*	0.000	2.069	6.055	1.031	2.029	6.052	1.024	2.026
B3LYP	0.000	2.169	6.083	1.050	2.047	6.078	1.039	2.045
PBE0	0.000	2.315	6.120	1.079	2.073	6.111	1.059	2.072
M06	0.000	2.363	6.144	1.067	2.062	6.148	1.054	2.064
M062X	0.000	2.724	6.277	1.193	2.173	6.267	1.140	2.175
B2-PLYP	0.000	2.907	6.576	1.753	2.726	6.550	1.709[b]	2.730

[a] Calculation converged to Mn^{V} $^3B_1$.

[b] Calculation converged to $[Mn^{IV}O^{\bullet}(P)]^+$ instead of $[Mn^{IV}O(P^{\bullet})]^+$.

References

(1) Addison, A. W.; Rao, T. N.; Reedijk, J.; van Rijn, J.; Verschoor, G. C. *J. Chem. Soc., Dalton Trans.* **1984**, 1349–1356.

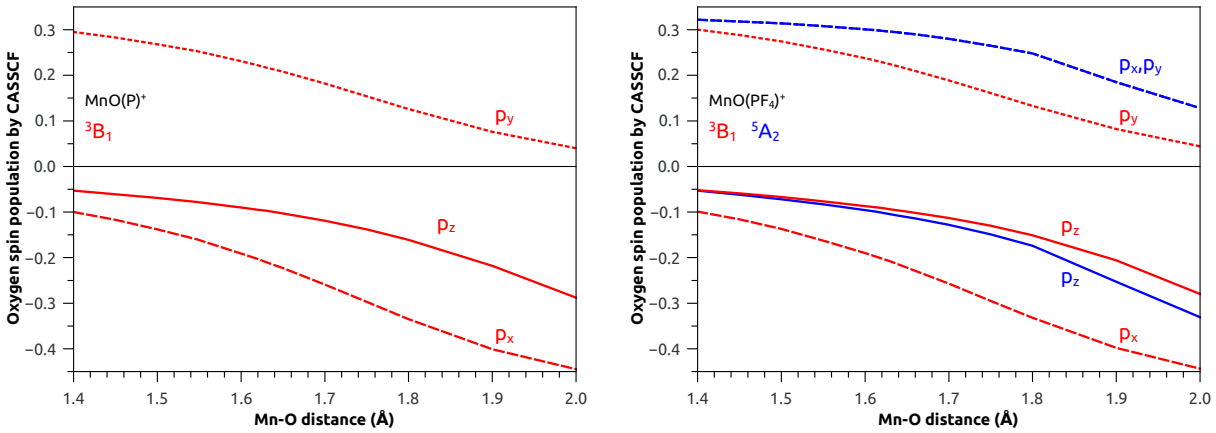

(a) (b)

Figure S2: Oxygen Mulliken spin population given by CASSCF as function of distance for (a) $MnO(P)^+$ and (b) $MnO(PF_4)^+$ split in atomic orbitals: $O(p_z)$ in solid line, $O(p_x)$ dashed and $O(p_y)$ dotted. Mn^V $^3B_1$ and Mn^{IV} $^5A_2$ are shown in red and blue respectively.

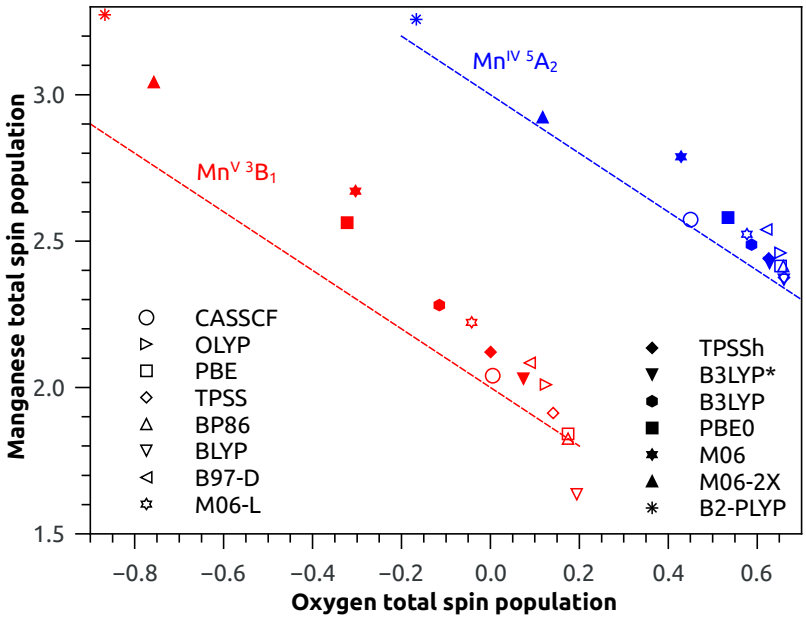

Figure S3: Total Mulliken spin population of Mn^V $^3B_1$ (red) and Mn^{IV} $^5A_2$ (blue) states of $MnO(P)^+$. Hybrid functionals are displayed with filled symbols and pure with open symbols.

Table S3: UPBE0/def2-TZVP structure of $Mn^{V}O(P)^{+}$ $^{1}A_{1}$.

38

Mn	0.0000000	0.0000000	0.3359758
O	0.0000000	0.0000000	1.8297508
N	1.3666362	-1.3559275	-0.1180308
N	1.3666362	1.3559275	-0.1180308
N	-1.3666362	-1.3559275	-0.1180308
N	-1.3666362	1.3559275	-0.1180308
C	-2.7259738	1.2000595	0.0537932
C	-1.201673	2.7071893	-0.3334657
C	-2.4542153	3.3812622	-0.3149287
C	-3.3978224	2.4498207	-0.0438664
C	-3.3712602	0.0000000	0.1966098
C	-2.7259738	-1.2000595	0.0537932
C	-3.3978224	-2.4498207	-0.0438664
C	-2.4542153	-3.3812622	-0.3149287
C	-1.201673	-2.7071893	-0.3334657
C	0.0000000	-3.3476252	-0.4787069
C	1.201673	-2.7071893	-0.3334657
C	2.4542153	-3.3812622	-0.3149287
C	3.3978224	-2.4498207	-0.0438664
C	2.7259738	-1.2000595	0.0537932
C	3.3712602	0.0000000	0.1966098
C	2.7259738	1.2000595	0.0537932
C	3.3978224	2.4498207	-0.0438664
C	2.4542153	3.3812622	-0.3149287
C	1.201673	2.7071893	-0.3334657
C	0.0000000	3.3476252	-0.4787069
H	0.0000000	4.4157677	-0.6506434
H	-2.577075	4.4417697	-0.4757792
H	-4.4649322	2.5777804	0.0588908
H	-4.4447354	0.0000000	0.3310094
H	-4.4649322	-2.5777804	0.0588908
H	-2.577075	-4.4417697	-0.4757792
H	0.0000000	-4.4157677	-0.6506434
H	2.577075	-4.4417697	-0.4757792
H	4.4649322	-2.5777804	0.0588908
H	4.4447354	0.0000000	0.3310094
H	4.4649322	2.5777804	0.0588908
H	2.577075	4.4417697	-0.4757792

Table S4: UPBE0/def2-TZVP structure of $Mn^{V}O(P)^{+}$ $^{3}B_{1}$.

38

Mn	0.0000000	0.0000000	0.2409885
O	0.0000000	0.0000000	1.9213835
N	-1.3912482	1.3912933	-0.0681899
N	-1.3912482	-1.3912933	-0.0681899
N	1.3912482	1.3912933	-0.0681899
N	1.3912482	-1.3912933	-0.0681899
C	2.7481694	-1.2145063	0.0735922
C	1.2138026	-2.7502026	-0.1838926
C	2.4714180	-3.4192178	-0.1528122
C	3.4202682	-2.4696054	0.0253513
C	3.3846814	0.0000000	0.1710942
C	2.7481694	1.2145063	0.0735922
C	3.4202682	2.4696054	0.0253513
C	2.4714180	3.4192178	-0.1528122
C	1.2138026	2.7502026	-0.1838926
C	0.0000000	3.3893630	-0.2674647
C	-1.2138026	2.7502026	-0.1838926
C	-2.4714180	3.4192178	-0.1528122
C	-3.4202682	2.4696054	0.0253513
C	-2.7481694	1.2145063	0.0735922
C	-3.3846814	0.0000000	0.1710942
C	-2.7481694	-1.2145063	0.0735922
C	-3.4202682	-2.4696054	0.0253513
C	-2.4714180	-3.4192178	-0.1528122
C	-1.2138026	-2.7502026	-0.1838926
C	0.0000000	-3.3893630	-0.2674647
H	0.0000000	-4.4679910	-0.3568392
H	2.5969971	-4.4873420	-0.2476566
H	4.4901844	-2.5928162	0.1011390
H	4.4618576	0.0000000	0.2769612
H	4.4901844	2.5928162	0.1011390
H	2.5969971	4.4873420	-0.2476566
H	0.0000000	4.4679910	-0.3568392
H	-2.5969971	4.4873420	-0.2476566
H	-4.4901844	2.5928162	0.1011390
H	-4.4618576	0.0000000	0.2769612
H	-4.4901844	-2.5928162	0.1011390
H	-2.5969971	-4.4873420	-0.2476566

Table S5: UPBE0/def2-TZVP structure of $Mn^{V}O(P)^{+}$ $^{3}B_{2}$.

38

Mn	0.0000000	0.0000000	0.2398943
O	0.0000000	0.0000000	1.9209673
N	-1.3928475	1.3918055	-0.0689909
N	-1.3928475	-1.3918055	-0.0689909
N	1.3928475	1.3918055	-0.0689909
N	1.3928475	-1.3918055	-0.0689909
C	2.7532527	-1.2138333	-0.1659549
C	1.2145989	-2.7503081	0.0550994
C	2.4698972	-3.4223331	0.0129490
C	3.4219339	-2.4716390	-0.1398901
C	3.3936287	0.0000000	-0.2364932
C	2.7532527	1.2138333	-0.1659549
C	3.4219339	2.4716390	-0.1398901
C	2.4698972	3.4223331	0.0129490
C	1.2145989	2.7503081	0.0550994
C	0.0000000	3.3880851	0.1397674
C	-1.2145989	2.7503081	0.0550994
C	-2.4698972	3.4223331	0.0129490
C	-3.4219339	2.4716390	-0.1398901
C	-2.7532527	1.2138333	-0.1659549
C	-3.3936287	0.0000000	-0.2364932
C	-2.7532527	-1.2138333	-0.1659549
C	-3.4219339	-2.4716390	-0.1398901
C	-2.4698972	-3.4223331	0.0129490
C	-1.2145989	-2.7503081	0.0550994
C	0.0000000	-3.3880851	0.1397674
H	0.0000000	-4.4665147	0.2319659
H	2.5916001	-4.4931924	0.0769463
H	4.4912327	-2.5960130	-0.2222164
H	4.4733494	0.0000000	-0.3115560
H	4.4912327	2.5960130	-0.2222164
H	2.5916001	4.4931924	0.0769463
H	0.0000000	4.4665147	0.2319659
H	-2.5916001	4.4931924	0.0769463
H	-4.4912327	2.5960130	-0.2222164
H	-4.4733494	0.0000000	-0.3115560
H	-4.4912327	-2.5960130	-0.2222164
H	-2.5916001	-4.4931924	0.0769463

Table S6: ROPBE0/def2-TZVP structure of $Mn^{V}O(P)^{+}$ $^{3}B_{1}$.

38

Mn	0.0000000000	0.0000000000	0.3374397498
O	0.0000000000	0.0000000000	1.8849707426
N	0.0000000000	1.9960350581	0.0793774172
N	0.0000000000	-1.9960350581	0.0793774172
N	-1.9010291885	0.0000000000	-0.1566704947
N	1.9010291885	0.0000000000	-0.1566704947
C	1.0866920216	-2.8291172611	0.1000984325
C	-1.0866920216	2.8291172611	0.1000984325
C	1.0866920216	2.8291172611	0.1000984325
C	-1.0866920216	-2.8291172611	0.1000984325
C	-0.6764186776	-4.1932222390	0.1774583304
C	0.6764186776	4.1932222390	0.1774583304
C	-0.6764186776	4.1932222390	0.1774583304
C	0.6764186776	-4.1932222390	0.1774583304
C	2.3851878504	-2.4110257236	-0.0398524824
C	-2.3851878504	2.4110257236	-0.0398524824
C	2.3851878504	2.4110257236	-0.0398524824
C	-2.3851878504	-2.4110257236	-0.0398524824
C	2.7474921514	-1.0965705653	-0.1859114989
C	-2.7474921514	1.0965705653	-0.1859114989
C	2.7474921514	1.0965705653	-0.1859114989
C	-2.7474921514	-1.0965705653	-0.1859114989
C	4.0976291567	-0.6766316737	-0.3237797871
C	-4.0976291567	0.6766316737	-0.3237797871
C	4.0976291567	0.6766316737	-0.3237797871
C	-4.0976291567	-0.6766316737	-0.3237797871
H	-3.1697276998	-3.1560310375	-0.0497077339
H	3.1697276998	3.1560310375	-0.0497077339
H	-3.1697276998	3.1560310375	-0.0497077339
H	3.1697276998	-3.1560310375	-0.0497077339
H	-1.3521818769	-5.0349002631	0.1986445473
H	1.3521818769	5.0349002631	0.1986445473
H	-1.3521818769	5.0349002631	0.1986445473
H	1.3521818769	-5.0349002631	0.1986445473
H	4.9371181842	-1.3519734733	-0.3927046922
H	-4.9371181842	1.3519734733	-0.3927046922
H	4.9371181842	1.3519734733	-0.3927046922
H	-4.9371181842	-1.3519734733	-0.3927046922

Table S7: UPBE0/def2-TZVP structure of $Mn^{IV}O(P^{\bullet})^{+}$ a_{2u} $^{5}A_{2}$.[a]

38

Mn	0.0000000	0.0000000	0.2001341
O	0.0000000	0.0000000	1.8138014
N	1.4187053	-1.4187031	-0.0572752
N	1.4187053	1.4187031	-0.0572752
N	-1.4187053	-1.4187031	-0.0572752
N	-1.4187053	1.4187031	-0.0572752
C	-2.7673676	1.2349850	-0.0529454
C	-1.2349854	2.7673655	-0.0530368
C	-2.4902050	3.4496909	-0.0600652
C	-3.4496921	2.4902049	-0.0600007
C	-3.3993750	0.0000000	-0.0466164
C	-2.7673676	-1.2349850	-0.0529454
C	-3.4496921	-2.4902049	-0.0600007
C	-2.4902050	-3.4496909	-0.0600652
C	-1.2349854	-2.7673655	-0.0530368
C	0.0000000	-3.3993729	-0.0467795
C	1.2349854	-2.7673655	-0.0530368
C	2.4902050	-3.4496909	-0.0600652
C	3.4496921	-2.4902049	-0.0600007
C	2.7673676	-1.2349850	-0.0529454
C	3.3993750	0.0000000	-0.0466164
C	2.7673676	1.2349850	-0.0529454
C	3.4496921	2.4902049	-0.0600007
C	2.4902050	3.4496909	-0.0600652
C	1.2349854	2.7673655	-0.0530368
C	0.0000000	3.3993729	-0.0467795
H	0.0000000	4.4830134	-0.0405404
H	-2.6124143	4.5223225	-0.0665896
H	-4.5223240	2.6124150	-0.0664623
H	-4.4830149	0.0000000	-0.0402810
H	-4.5223240	-2.6124150	-0.0664623
H	-2.6124143	-4.5223225	-0.0665896
H	0.0000000	-4.4830134	-0.0405404
H	2.6124143	-4.5223225	-0.0665896
H	4.5223240	-2.6124150	-0.0664623
H	4.4830149	0.0000000	-0.0402810
H	4.5223240	2.6124150	-0.0664623
H	2.6124143	4.5223225	-0.0665896

[a]Imaginary mode at $1390.47i$ cm^{-1}

Table S8: UPBE0/def2-TZVP structure of $Mn^{IV}O(P^{\bullet})^{+}$ a_{2u} $^{3}B_{1}$.[a]

38

Mn	0.0000000	0.0000000	0.3318127
O	0.0000000	0.0000000	1.8750978
N	0.0000000	1.9541734	-0.0902162
N	0.0000000	-1.9541734	-0.0902162
N	-2.0237498	0.0000000	0.0496567
N	2.0237498	0.0000000	0.0496567
C	1.0835388	-2.7863962	-0.1217593
C	-1.0835388	2.7863962	-0.1217593
C	1.0835388	2.7863962	-0.1217593
C	-1.0835388	-2.7863962	-0.1217593
C	-0.6794283	-4.1491088	-0.2120400
C	0.6794283	4.1491088	-0.2120400
C	-0.6794283	4.1491088	-0.2120400
C	0.6794283	-4.1491088	-0.2120400
C	2.4103427	-2.3885400	-0.0387959
C	-2.4103427	2.3885400	-0.0387959
C	2.4103427	2.3885400	-0.0387959
C	-2.4103427	-2.3885400	-0.0387959
C	2.8502433	-1.0782602	0.0430148
C	-2.8502433	1.0782602	0.0430148
C	2.8502433	1.0782602	0.0430148
C	-2.8502433	-1.0782602	0.0430148
C	4.2238338	-0.6779127	0.0593208
C	-4.2238338	0.6779127	0.0593208
C	4.2238338	0.6779127	0.0593208
C	-4.2238338	-0.6779127	0.0593208
H	-3.1610642	-3.1699274	-0.0543470
H	3.1610642	3.1699274	-0.0543470
H	-3.1610642	3.1699274	-0.0543470
H	3.1610642	-3.1699274	-0.0543470
H	-1.3519251	-4.9922793	-0.2614281
H	1.3519251	4.9922793	-0.2614281
H	-1.3519251	4.9922793	-0.2614281
H	1.3519251	-4.9922793	-0.2614281
H	5.0682285	-1.3506860	0.0545869
H	-5.0682285	1.3506860	0.0545869
H	5.0682285	1.3506860	0.0545869
H	-5.0682285	-1.3506860	0.0545869

[a]Imaginary mode at $1626.77i$ cm^{-1}

Table S9: UPBE0/def2-TZVP structure of $Mn^{IV}O(P^{\bullet})^{+}$ a_{2u} $^{3}B_{2}$.[a]

38

Mn	0.0000000	0.0000000	0.3313576
O	0.0000000	0.0000000	1.8746689
N	0.0000000	2.0237162	0.0492823
N	0.0000000	-2.0237162	0.0492823
N	-1.9542104	0.0000000	-0.0905254
N	1.9542104	0.0000000	-0.0905254
C	1.0782627	-2.8502218	0.0427598
C	-1.0782627	2.8502218	0.0427598
C	1.0782627	2.8502218	0.0427598
C	-1.0782627	-2.8502218	0.0427598
C	-0.6779078	-4.2238098	0.0592535
C	0.6779078	4.2238098	0.0592535
C	-0.6779078	4.2238098	0.0592535
C	0.6779078	-4.2238098	0.0592535
C	2.3885356	-2.4103202	-0.0388975
C	-2.3885356	2.4103202	-0.0388975
C	2.3885356	2.4103202	-0.0388975
C	-2.3885356	-2.4103202	-0.0388975
C	2.7864504	-1.0835403	-0.1218705
C	-2.7864504	1.0835403	-0.1218705
C	2.7864504	1.0835403	-0.1218705
C	-2.7864504	-1.0835403	-0.1218705
C	4.1491923	-0.6794228	-0.2117933
C	-4.1491923	0.6794228	-0.2117933
C	4.1491923	0.6794228	-0.2117933
C	-4.1491923	-0.6794228	-0.2117933
H	-3.1699043	-3.1610754	-0.0542220
H	3.1699043	3.1610754	-0.0542220
H	-3.1699043	3.1610754	-0.0542220
H	3.1699043	-3.1610754	-0.0542220
H	-1.3506809	-5.0682065	0.0547201
H	1.3506809	5.0682065	0.0547201
H	-1.3506809	5.0682065	0.0547201
H	1.3506809	-5.0682065	0.0547201
H	4.9923881	-1.3519121	-0.2608353
H	-4.9923881	1.3519121	-0.2608353
H	4.9923881	1.3519121	-0.2608353
H	-4.9923881	-1.3519121	-0.2608353

[a]Imaginary mode at $1627.20i$ cm^{-1}

Table S10: UPBE0/def2-TZVP structure of $Mn^{IV}O(P^{\bullet})^{+}$ a_{2u} $^{1}B_{1}$.[a]

38

Mn	0.0000000	0.0000000	0.3321255
O	0.0000000	0.0000000	1.8755416
N	0.0000000	1.9549768	-0.0873974
N	0.0000000	-1.9549768	-0.0873974
N	-2.0234730	0.0000000	0.0503508
N	2.0234730	0.0000000	0.0503508
C	1.0836049	-2.7870023	-0.1198649
C	-1.0836049	2.7870023	-0.1198649
C	1.0836049	2.7870023	-0.1198649
C	-1.0836049	-2.7870023	-0.1198649
C	-0.6794404	-4.1496655	-0.2108612
C	0.6794404	4.1496655	-0.2108612
C	-0.6794404	4.1496655	-0.2108612
C	0.6794404	-4.1496655	-0.2108612
C	2.4103833	-2.3888202	-0.0380697
C	-2.4103833	2.3888202	-0.0380697
C	2.4103833	2.3888202	-0.0380697
C	-2.4103833	-2.3888202	-0.0380697
C	2.8499559	-1.0782742	0.0426427
C	-2.8499559	1.0782742	0.0426427
C	2.8499559	1.0782742	0.0426427
C	-2.8499559	-1.0782742	0.0426427
C	4.2235188	-0.6779399	0.0570153
C	-4.2235188	0.6779399	0.0570153
C	4.2235188	0.6779399	0.0570153
C	-4.2235188	-0.6779399	0.0570153
H	-3.1613517	-3.1699437	-0.0541996
H	3.1613517	3.1699437	-0.0541996
H	-3.1613517	3.1699437	-0.0541996
H	3.1613517	-3.1699437	-0.0541996
H	-1.3519136	-4.9928006	-0.2611556
H	1.3519136	4.9928006	-0.2611556
H	-1.3519136	4.9928006	-0.2611556
H	1.3519136	-4.9928006	-0.2611556
H	5.0678991	-1.3507221	0.0510995
H	-5.0678991	1.3507221	0.0510995
H	5.0678991	1.3507221	0.0510995
H	-5.0678991	-1.3507221	0.0510995

[a]Imaginary mode at $1600.22i$ cm^{-1}

Table S11: UPBE0/def2-TZVP structure of $Mn^{IV}O(P^{\bullet})^{+}$ a_{2u} $^{1}B_{2}$.[a]

38

Mn	0.0000000	0.0000000	0.3321101
O	0.0000000	0.0000000	1.8755284
N	0.0000000	2.0234567	0.0503552
N	0.0000000	-2.0234567	0.0503552
N	-1.9549978	0.0000000	-0.0873752
N	1.9549978	0.0000000	-0.0873752
C	1.0782726	-2.8499415	0.0426599
C	-1.0782726	2.8499415	0.0426599
C	1.0782726	2.8499415	0.0426599
C	-1.0782726	-2.8499415	0.0426599
C	-0.6779360	-4.2235047	0.0570518
C	0.6779360	4.2235047	0.0570518
C	-0.6779360	4.2235047	0.0570518
C	0.6779360	-4.2235047	0.0570518
C	2.3888185	-2.4103699	-0.0380606
C	-2.3888185	2.4103699	-0.0380606
C	2.3888185	2.4103699	-0.0380606
C	-2.3888185	-2.4103699	-0.0380606
C	2.7870206	-1.0836016	-0.1198669
C	-2.7870206	1.0836016	-0.1198669
C	2.7870206	1.0836016	-0.1198669
C	-2.7870206	-1.0836016	-0.1198669
C	4.1496831	-0.6794360	-0.2109084
C	-4.1496831	0.6794360	-0.2109084
C	4.1496831	0.6794360	-0.2109084
C	-4.1496831	-0.6794360	-0.2109084
H	-3.1699340	-3.1613506	-0.0541897
H	3.1699340	3.1613506	-0.0541897
H	-3.1699340	3.1613506	-0.0541897
H	3.1699340	-3.1613506	-0.0541897
H	-1.3507253	-5.0678800	0.0511586
H	1.3507253	5.0678800	0.0511586
H	-1.3507253	5.0678800	0.0511586
H	1.3507253	-5.0678800	0.0511586
H	4.9928087	-1.3519181	-0.2612444
H	-4.9928087	1.3519181	-0.2612444
H	4.9928087	1.3519181	-0.2612444
H	-4.9928087	-1.3519181	-0.2612444

[a]Imaginary mode at $1600.29i$ cm^{-1}

Table S12: UPBE0/def2-TZVP structure of $Mn^{IV}O(P^{\bullet})^{+}$ a_{1u} $^{5}A_{1}$.

38

Mn	0.0000000	0.0000000	0.2108153
O	0.0000000	0.0000000	1.8284676
N	1.4084443	-1.4084442	-0.0609199
N	1.4084443	1.4084442	-0.0609199
N	-1.4084443	-1.4084442	-0.0609199
N	-1.4084443	1.4084442	-0.0609199
C	-2.7578110	1.2205520	-0.0536899
C	-1.2205520	2.7578109	-0.0536956
C	-2.4962481	3.4451858	-0.0613820
C	-3.4451859	2.4962481	-0.0613781
C	-3.4012328	0.0000000	-0.0456947
C	-2.7578110	-1.2205520	-0.0536899
C	-3.4451859	-2.4962481	-0.0613781
C	-2.4962481	-3.4451858	-0.0613820
C	-1.2205520	-2.7578109	-0.0536956
C	0.0000000	-3.4012327	-0.0457045
C	1.2205520	-2.7578109	-0.0536956
C	2.4962481	-3.4451858	-0.0613820
C	3.4451859	-2.4962481	-0.0613781
C	2.7578110	-1.2205520	-0.0536899
C	3.4012328	0.0000000	-0.0456947
C	2.7578110	1.2205520	-0.0536899
C	3.4451859	2.4962481	-0.0613781
C	2.4962481	3.4451858	-0.0613820
C	1.2205520	2.7578109	-0.0536956
C	0.0000000	3.4012327	-0.0457045
H	0.0000000	4.4833556	-0.0380976
H	-2.6132095	4.5185088	-0.0674865
H	-4.5185088	2.6132095	-0.0674787
H	-4.4833557	0.0000000	-0.0380833
H	-4.5185088	-2.6132095	-0.0674787
H	-2.6132095	-4.5185088	-0.0674865
H	0.0000000	-4.4833556	-0.0380976
H	2.6132095	-4.5185088	-0.0674865
H	4.5185088	-2.6132095	-0.0674787
H	4.4833557	0.0000000	-0.0380833
H	4.5185088	2.6132095	-0.0674787
H	2.6132095	4.5185088	-0.0674865

Table S13: UPBE0/def2-TZVP structure of $Mn^{IV}O(P^{\bullet})^{+}$ a_{1u} $^{3}B_{1}$.

38

Mn	0.0000000	0.0000000	0.3450546
O	0.0000000	0.0000000	1.8933455
N	0.0000000	2.0057686	0.0531198
N	0.0000000	-2.0057686	0.0531198
N	-1.9396194	0.0000000	-0.0973366
N	1.9396194	0.0000000	-0.0973366
C	1.0807996	-2.8299451	0.0390374
C	-1.0807996	2.8299451	0.0390374
C	1.0807996	2.8299451	0.0390374
C	-1.0807996	-2.8299451	0.0390374
C	-0.6708745	-4.2212546	0.0535520
C	0.6708745	4.2212546	0.0535520
C	-0.6708745	4.2212546	0.0535520
C	0.6708745	-4.2212546	0.0535520
C	2.3914621	-2.4093279	-0.0378063
C	-2.3914621	2.4093279	-0.0378063
C	2.3914621	2.4093279	-0.0378063
C	-2.3914621	-2.4093279	-0.0378063
C	2.7715723	-1.0871155	-0.1194238
C	-2.7715723	1.0871155	-0.1194238
C	2.7715723	1.0871155	-0.1194238
C	-2.7715723	-1.0871155	-0.1194238
C	4.1532111	-0.6710342	-0.2102435
C	-4.1532111	0.6710342	-0.2102435
C	4.1532111	0.6710342	-0.2102435
C	-4.1532111	-0.6710342	-0.2102435
H	-3.1703954	-3.1604655	-0.0525516
H	3.1703954	3.1604655	-0.0525516
H	-3.1703954	3.1604655	-0.0525516
H	3.1703954	-3.1604655	-0.0525516
H	-1.3480559	-5.0622373	0.0475409
H	1.3480559	5.0622373	0.0475409
H	-1.3480559	5.0622373	0.0475409
H	1.3480559	-5.0622373	0.0475409
H	4.9930411	-1.3480160	-0.2575968
H	-4.9930411	1.3480160	-0.2575968
H	4.9930411	1.3480160	-0.2575968
H	-4.9930411	-1.3480160	-0.2575968

Table S14: UPBE0/def2-TZVP structure of $Mn^{IV}O(P^{\bullet})^{+}$ a_{1u} $^{3}B_{2}$.

38

Mn	0.0000000	0.0000000	0.3450434
O	0.0000000	0.0000000	1.8933429
N	0.0000000	1.9396234	-0.0973262
N	0.0000000	-1.9396234	-0.0973262
N	-2.0057664	0.0000000	0.0531029
N	2.0057664	0.0000000	0.0531029
C	1.0871154	-2.7715769	-0.1194085
C	-1.0871154	2.7715769	-0.1194085
C	1.0871154	2.7715769	-0.1194085
C	-1.0871154	-2.7715769	-0.1194085
C	-0.6710342	-4.1532163	-0.2102163
C	0.6710342	4.1532163	-0.2102163
C	-0.6710342	4.1532163	-0.2102163
C	0.6710342	-4.1532163	-0.2102163
C	2.4093276	-2.3914635	-0.0378057
C	-2.4093276	2.3914635	-0.0378057
C	2.4093276	2.3914635	-0.0378057
C	-2.4093276	-2.3914635	-0.0378057
C	2.8299440	-1.0807998	0.0390213
C	-2.8299440	1.0807998	0.0390213
C	2.8299440	1.0807998	0.0390213
C	-2.8299440	-1.0807998	0.0390213
C	4.2212525	-0.6708747	0.0535243
C	-4.2212525	0.6708747	0.0535243
C	4.2212525	0.6708747	0.0535243
C	-4.2212525	-0.6708747	0.0535243
H	-3.1604652	-3.1703969	-0.0525479
H	3.1604652	3.1703969	-0.0525479
H	-3.1604652	3.1703969	-0.0525479
H	3.1604652	-3.1703969	-0.0525479
H	-1.3480159	-4.9930467	-0.2575646
H	1.3480159	4.9930467	-0.2575646
H	-1.3480159	4.9930467	-0.2575646
H	1.3480159	-4.9930467	-0.2575646
H	5.0622358	-1.3480553	0.0475125
H	-5.0622358	1.3480553	0.0475125
H	5.0622358	1.3480553	0.0475125
H	-5.0622358	-1.3480553	0.0475125

Table S15: UPBE0/def2-TZVP structure of $Mn^{IV}O(P^{\bullet})^{+}$ a_{1u} $^{1}B_{1}$.

38

Mn	0.0000000	0.0000000	0.3436668
O	0.0000000	0.0000000	1.8908313
N	0.0000000	2.0068599	0.0520259
N	0.0000000	-2.0068599	0.0520259
N	-1.9385697	0.0000000	-0.1011614
N	1.9385697	0.0000000	-0.1011614
C	1.0808072	-2.8306732	0.0423322
C	-1.0808072	2.8306732	0.0423322
C	1.0808072	2.8306732	0.0423322
C	-1.0808072	-2.8306732	0.0423322
C	-0.6709227	-4.2219429	0.0650257
C	0.6709227	4.2219429	0.0650257
C	-0.6709227	4.2219429	0.0650257
C	0.6709227	-4.2219429	0.0650257
C	2.3911233	-2.4094835	-0.0389703
C	-2.3911233	2.4094835	-0.0389703
C	2.3911233	2.4094835	-0.0389703
C	-2.3911233	-2.4094835	-0.0389703
C	2.7703805	-1.0872374	-0.1248144
C	-2.7703805	1.0872374	-0.1248144
C	2.7703805	1.0872374	-0.1248144
C	-2.7703805	-1.0872374	-0.1248144
C	4.1516533	-0.6710752	-0.2197266
C	-4.1516533	0.6710752	-0.2197266
C	4.1516533	0.6710752	-0.2197266
C	-4.1516533	-0.6710752	-0.2197266
H	-3.1705604	-3.1601145	-0.0528118
H	3.1705604	3.1601145	-0.0528118
H	-3.1705604	3.1601145	-0.0528118
H	3.1705604	-3.1601145	-0.0528118
H	-1.3480210	-5.0630147	0.0639867
H	1.3480210	5.0630147	0.0639867
H	-1.3480210	5.0630147	0.0639867
H	1.3480210	-5.0630147	0.0639867
H	4.9914198	-1.3479948	-0.2690782
H	-4.9914198	1.3479948	-0.2690782
H	4.9914198	1.3479948	-0.2690782
H	-4.9914198	-1.3479948	-0.2690782

Table S16: UPBE0/def2-TZVP structure of $Mn^{IV}O(P^{\bullet})^{+}$ a_{1u} $^{1}B_{2}$.

38

Mn	0.0000000	0.0000000	0.3437186
O	0.0000000	0.0000000	1.8908864
N	0.0000000	1.9385980	-0.1010464
N	0.0000000	-1.9385980	-0.1010464
N	-2.0068658	0.0000000	0.0519582
N	2.0068658	0.0000000	0.0519582
C	1.0872353	-2.7704127	-0.1245937
C	-1.0872353	2.7704127	-0.1245937
C	1.0872353	2.7704127	-0.1245937
C	-1.0872353	-2.7704127	-0.1245937
C	-0.6710749	-4.1517024	-0.2192579
C	0.6710749	4.1517024	-0.2192579
C	-0.6710749	4.1517024	-0.2192579
C	0.6710749	-4.1517024	-0.2192579
C	2.4094876	-2.3911352	-0.0389605
C	-2.4094876	2.3911352	-0.0389605
C	2.4094876	2.3911352	-0.0389605
C	-2.4094876	-2.3911352	-0.0389605
C	2.8306802	-1.0808073	0.0421236
C	-2.8306802	1.0808073	0.0421236
C	2.8306802	1.0808073	0.0421236
C	-2.8306802	-1.0808073	0.0421236
C	4.2219529	-0.6709227	0.0645162
C	-4.2219529	0.6709227	0.0645162
C	4.2219529	0.6709227	0.0645162
C	-4.2219529	-0.6709227	0.0645162
H	-3.1601230	-3.1705676	-0.0527994
H	3.1601230	3.1705676	-0.0527994
H	-3.1601230	3.1705676	-0.0527994
H	3.1601230	-3.1705676	-0.0527994
H	-1.3479960	-4.9914770	-0.2684535
H	1.3479960	4.9914770	-0.2684535
H	-1.3479960	4.9914770	-0.2684535
H	1.3479960	-4.9914770	-0.2684535
H	5.0630236	-1.3480219	0.0633182
H	-5.0630236	1.3480219	0.0633182
H	5.0630236	1.3480219	0.0633182
H	-5.0630236	-1.3480219	0.0633182

Table S17: UPBE0/def2-TZVP structure of $Mn^{V}O(PF_4)^+$ $^1A_1$.

38

Mn	0.0000000	0.0000000	0.4351748
O	0.0000000	0.0000000	1.9347961
N	1.3666965	-1.3560822	-0.0273431
N	1.3666965	1.3560822	-0.0273431
N	-1.3666965	-1.3560822	-0.0273431
N	-1.3666965	1.3560822	-0.0273431
C	-2.7283309	1.2122894	0.1346321
C	-1.2136918	2.7114463	-0.2239304
C	-2.4567344	3.3914012	-0.2035813
C	-3.4053110	2.4535362	0.0450542
C	-3.3563338	0.0000000	0.2672615
C	-2.7283309	-1.2122894	0.1346321
C	-3.4053110	-2.4535362	0.0450542
C	-2.4567344	-3.3914012	-0.2035813
C	-1.2136918	-2.7114463	-0.2239304
C	0.0000000	-3.3351505	-0.3588674
C	1.2136918	-2.7114463	-0.2239304
C	2.4567344	-3.3914012	-0.2035813
C	3.4053110	-2.4535362	0.0450542
C	2.7283309	-1.2122894	0.1346321
C	3.3563338	0.0000000	0.2672615
C	2.7283309	1.2122894	0.1346321
C	3.4053110	2.4535362	0.0450542
C	2.4567344	3.3914012	-0.2035813
C	1.2136918	2.7114463	-0.2239304
C	0.0000000	3.3351505	-0.3588674
F	0.0000000	4.6411053	-0.5626527
H	-2.5792288	4.4531224	-0.3491960
H	-4.4722447	2.5810741	0.1394592
F	-4.6664132	0.0000000	0.4390838
H	-4.4722447	-2.5810741	0.1394592
H	-2.5792288	-4.4531224	-0.3491960
F	0.0000000	-4.6411053	-0.5626527
H	2.5792288	-4.4531224	-0.3491960
H	4.4722447	-2.5810741	0.1394592
F	4.6664132	0.0000000	0.4390838
H	4.4722447	2.5810741	0.1394592
H	2.5792288	4.4531224	-0.3491960

Table S18: ROPBE0/def2-TZVP structure of $Mn^{V}O(PF_4)^+$ $^3B_1$.

38

Mn	0.0000000000	0.0000000000	0.3408109308
O	0.0000000000	0.0000000000	1.8933685413
N	0.0000000000	1.9960046560	0.0616847209
N	0.0000000000	-1.9960046560	0.0616847209
N	-1.9074420787	0.0000000000	-0.1568206297
N	1.9074420787	0.0000000000	-0.1568206297
C	1.0788376271	-2.8393732946	0.0581885647
C	-1.0788376271	2.8393732946	0.0581885647
C	1.0788376271	2.8393732946	0.0581885647
C	-1.0788376271	-2.8393732946	0.0581885647
C	-0.6782702006	-4.2019923373	0.0789568290
C	0.6782702006	4.2019923373	0.0789568290
C	-0.6782702006	4.2019923373	0.0789568290
C	0.6782702006	-4.2019923373	0.0789568290
C	2.3761102989	-2.3999292793	-0.0449511192
C	-2.3761102989	2.3999292793	-0.0449511192
C	2.3761102989	2.3999292793	-0.0449511192
C	-2.3761102989	-2.3999292793	-0.0449511192
C	2.7647716260	-1.0870820793	-0.1526629662
C	-2.7647716260	1.0870820793	-0.1526629662
C	2.7647716260	1.0870820793	-0.1526629662
C	-2.7647716260	-1.0870820793	-0.1526629662
C	4.1185794611	-0.6781925047	-0.2207210141
C	-4.1185794611	0.6781925047	-0.2207210141
C	4.1185794611	0.6781925047	-0.2207210141
C	-4.1185794611	-0.6781925047	-0.2207210141
F	-3.3304222637	-3.3148617675	-0.0506056299
F	3.3304222637	3.3148617675	-0.0506056299
F	-3.3304222637	3.3148617675	-0.0506056299
F	3.3304222637	-3.3148617675	-0.0506056299
H	-1.3527208502	-5.0437047382	0.0678559828
H	1.3527208502	5.0437047382	0.0678559828
H	-1.3527208502	5.0437047382	0.0678559828
H	1.3527208502	-5.0437047382	0.0678559828
H	4.9603708505	-1.3520083495	-0.2470373107
H	-4.9603708505	1.3520083495	-0.2470373107
H	4.9603708505	1.3520083495	-0.2470373107
H	-4.9603708505	-1.3520083495	-0.2470373107

Table S19: UPBE0/def2-TZVP structure of $Mn^{IV}O(PF_4^{\bullet})^+$ a_{2u} $^5A_2$.

38

Mn	0.0000000000	0.0000000000	0.1979729000
O	0.0000000000	0.0000000000	1.8107750000
N	1.4196765000	-1.4196735000	-0.0612682000
N	1.4196765000	1.4196735000	-0.0612682000
N	-1.4196765000	-1.4196735000	-0.0612682000
N	-1.4196765000	1.4196735000	-0.0612682000
C	-2.7690236000	1.2468156000	-0.0546566000
C	-1.2468161000	2.7690211000	-0.0547877000
C	-2.4930191000	3.4547405000	-0.0591351000
C	-3.4547418000	2.4930190000	-0.0590456000
C	-3.3844407000	0.0000000000	-0.0469642000
C	-2.7690236000	-1.2468156000	-0.0546566000
C	-3.4547418000	-2.4930190000	-0.0590456000
C	-2.4930191000	-3.4547405000	-0.0591351000
C	-1.2468161000	-2.7690211000	-0.0547877000
C	0.0000000000	-3.3844383000	-0.0471933000
C	1.2468161000	-2.7690211000	-0.0547877000
C	2.4930191000	-3.4547405000	-0.0591351000
C	3.4547418000	-2.4930190000	-0.0590456000
C	2.7690236000	-1.2468156000	-0.0546566000
C	3.3844407000	0.0000000000	-0.0469642000
C	2.7690236000	1.2468156000	-0.0546566000
C	3.4547418000	2.4930190000	-0.0590456000
C	2.4930191000	3.4547405000	-0.0591351000
C	1.2468161000	2.7690211000	-0.0547877000
C	0.0000000000	3.3844383000	-0.0471933000
F	0.0000000000	4.6988426000	-0.0380334000
H	-2.6171137000	4.5261165000	-0.0642702000
H	-4.5261182000	2.6171147000	-0.0640966000
F	-4.6988437000	0.0000000000	-0.0376630000
H	-4.5261182000	-2.6171147000	-0.0640966000
H	-2.6171137000	-4.5261165000	-0.0642702000
F	0.0000000000	-4.6988426000	-0.0380334000
H	2.6171137000	-4.5261165000	-0.0642702000
H	4.5261182000	-2.6171147000	-0.0640966000
F	4.6988437000	0.0000000000	-0.0376630000
H	4.5261182000	2.6171147000	-0.0640966000
H	2.6171137000	4.5261165000	-0.0642702000

Table S20: UPBE0/def2-TZVP structure of $Mn^{IV}O(PF_4^{\bullet})^+$ a_{2u} $^3B_1$.

38

Mn	0.0000000000	0.0000000000	0.3281117000
O	0.0000000000	0.0000000000	1.8710439000
N	0.0000000000	1.9557100000	-0.0917696000
N	0.0000000000	-1.9557100000	-0.0917696000
N	-2.0245146000	0.0000000000	0.0437351000
N	2.0245146000	0.0000000000	0.0437351000
C	1.0764851000	-2.7963631000	-0.1220188000
C	-1.0764851000	2.7963631000	-0.1220188000
C	1.0764851000	2.7963631000	-0.1220188000
C	-1.0764851000	-2.7963631000	-0.1220188000
C	-0.6808789000	-4.1556188000	-0.2064090000
C	0.6808789000	4.1556188000	-0.2064090000
C	-0.6808789000	4.1556188000	-0.2064090000
C	0.6808789000	-4.1556188000	-0.2064090000
C	2.3996694000	-2.3771439000	-0.0382332000
C	-2.3996694000	2.3771439000	-0.0382332000
C	2.3996694000	2.3771439000	-0.0382332000
C	-2.3996694000	-2.3771439000	-0.0382332000
C	2.8596628000	-1.0709515000	0.0403266000
C	-2.8596628000	1.0709515000	0.0403266000
C	2.8596628000	1.0709515000	0.0403266000
C	-2.8596628000	-1.0709515000	0.0403266000
C	4.2290113000	-0.6795746000	0.0552050000
C	-4.2290113000	0.6795746000	0.0552050000
C	4.2290113000	0.6795746000	0.0552050000
C	-4.2290113000	-0.6795746000	0.0552050000
F	-3.3126580000	-3.3232460000	-0.0518962000
F	3.3126580000	3.3232460000	-0.0518962000
F	-3.3126580000	3.3232460000	-0.0518962000
F	3.3126580000	-3.3232460000	-0.0518962000
H	-1.3504516000	-4.9998446000	-0.2529408000
H	1.3504516000	4.9998446000	-0.2529408000
H	-1.3504516000	4.9998446000	-0.2529408000
H	1.3504516000	-4.9998446000	-0.2529408000
H	5.0736379000	-1.3503790000	0.0501948000
H	-5.0736379000	1.3503790000	0.0501948000
H	5.0736379000	1.3503790000	0.0501948000
H	-5.0736379000	-1.3503790000	0.0501948000

Table S21: UPBE0/def2-TZVP structure of $Mn^{IV}O(PF_4^{\bullet})^+$ a_{2u} $^3B_2$.

38

Mn	0.0000000	0.0000000	0.3279683
O	0.0000000	0.0000000	1.8709049
N	0.0000000	2.0244887	0.0436279
N	0.0000000	-2.0244887	0.0436279
N	-1.9557361	0.0000000	-0.0918525
N	1.9557361	0.0000000	-0.0918525
C	1.0709536	-2.8596427	0.0402232
C	-1.0709536	2.8596427	0.0402232
C	1.0709536	2.8596427	0.0402232
C	-1.0709536	-2.8596427	0.0402232
C	-0.6795736	-4.2289888	0.0550932
C	0.6795736	4.2289888	0.0550932
C	-0.6795736	4.2289888	0.0550932
C	0.6795736	-4.2289888	0.0550932
C	2.3771581	-2.3996646	-0.0382546
C	-2.3771581	2.3996646	-0.0382546
C	2.3771581	2.3996646	-0.0382546
C	-2.3771581	-2.3996646	-0.0382546
C	2.7963982	-1.0764878	-0.1219984
C	-2.7963982	1.0764878	-0.1219984
C	2.7963982	1.0764878	-0.1219984
C	-2.7963982	-1.0764878	-0.1219984
C	4.1556630	-0.6808784	-0.2062317
C	-4.1556630	0.6808784	-0.2062317
C	4.1556630	0.6808784	-0.2062317
C	-4.1556630	-0.6808784	-0.2062317
F	-3.3232540	-3.3126774	-0.0518419
F	3.3232540	3.3126774	-0.0518419
F	-3.3232540	3.3126774	-0.0518419
F	3.3232540	-3.3126774	-0.0518419
H	-1.3503752	-5.0736180	0.0500862
H	1.3503752	5.0736180	0.0500862
H	-1.3503752	5.0736180	0.0500862
H	1.3503752	-5.0736180	0.0500862
H	4.9998943	-1.3504505	-0.2526820
H	-4.9998943	1.3504505	-0.2526820
H	4.9998943	1.3504505	-0.2526820
H	-4.9998943	-1.3504505	-0.2526820

Table S22: UPBE0/def2-TZVP structure of $Mn^{IV}O(PF_4^{\bullet})^+$ a_{2u} $^1B_1$.

38

Mn	0.0000000	0.0000000	0.3282310
O	0.0000000	0.0000000	1.8709299
N	0.0000000	1.9565000	-0.0885582
N	0.0000000	-1.9565000	-0.0885582
N	-2.0243364	0.0000000	0.0443131
N	2.0243364	0.0000000	0.0443131
C	1.0765880	-2.7968925	-0.1202283
C	-1.0765880	2.7968925	-0.1202283
C	1.0765880	2.7968925	-0.1202283
C	-1.0765880	-2.7968925	-0.1202283
C	-0.6809063	-4.1560254	-0.2060736
C	0.6809063	4.1560254	-0.2060736
C	-0.6809063	4.1560254	-0.2060736
C	0.6809063	-4.1560254	-0.2060736
C	2.3997641	-2.3774313	-0.0374110
C	-2.3997641	2.3774313	-0.0374110
C	2.3997641	2.3774313	-0.0374110
C	-2.3997641	-2.3774313	-0.0374110
C	2.8594626	-1.0710199	0.0401989
C	-2.8594626	1.0710199	0.0401989
C	2.8594626	1.0710199	0.0401989
C	-2.8594626	-1.0710199	0.0401989
C	4.2287606	-0.6795997	0.0537497
C	-4.2287606	0.6795997	0.0537497
C	4.2287606	0.6795997	0.0537497
C	-4.2287606	-0.6795997	0.0537497
F	-3.3130317	-3.3233752	-0.0518425
F	3.3130317	3.3233752	-0.0518425
F	-3.3130317	3.3233752	-0.0518425
F	3.3130317	-3.3233752	-0.0518425
H	-1.3504644	-5.0001859	-0.2540265
H	1.3504644	5.0001859	-0.2540265
H	-1.3504644	5.0001859	-0.2540265
H	1.3504644	-5.0001859	-0.2540265
H	5.0733921	-1.3503927	0.0479656
H	-5.0733921	1.3503927	0.0479656
H	5.0733921	1.3503927	0.0479656
H	-5.0733921	-1.3503927	0.0479656

Table S23: UPBE0/def2-TZVP structure of $Mn^{IV}O(PF_4^{\bullet})^+$ a_{2u} $^1B_2$.

38

Mn	0.0000000	0.0000000	0.3281452
O	0.0000000	0.0000000	1.8708482
N	0.0000000	2.0242949	0.0442475
N	0.0000000	-2.0242949	0.0442475
N	-1.9565410	0.0000000	-0.0885618
N	1.9565410	0.0000000	-0.0885618
C	1.0710212	-2.8594265	0.0401665
C	-1.0710212	2.8594265	0.0401665
C	1.0710212	2.8594265	0.0401665
C	-1.0710212	-2.8594265	0.0401665
C	-0.6795990	-4.2287214	0.0537580
C	0.6795990	4.2287214	0.0537580
C	-0.6795990	4.2287214	0.0537580
C	0.6795990	-4.2287214	0.0537580
C	2.3774439	-2.3997531	-0.0374096
C	-2.3774439	2.3997531	-0.0374096
C	2.3774439	2.3997531	-0.0374096
C	-2.3774439	-2.3997531	-0.0374096
C	2.7969237	-1.0765860	-0.1202296
C	-2.7969237	1.0765860	-0.1202296
C	2.7969237	1.0765860	-0.1202296
C	-2.7969237	-1.0765860	-0.1202296
C	4.1560628	-0.6809042	-0.2060640
C	-4.1560628	0.6809042	-0.2060640
C	4.1560628	0.6809042	-0.2060640
C	-4.1560628	-0.6809042	-0.2060640
F	-3.3233717	-3.3130370	-0.0518052
F	3.3233717	3.3130370	-0.0518052
F	-3.3233717	3.3130370	-0.0518052
F	3.3233717	-3.3130370	-0.0518052
H	-1.3503978	-5.0733482	0.0480005
H	1.3503978	5.0733482	0.0480005
H	-1.3503978	5.0733482	0.0480005
H	1.3503978	-5.0733482	0.0480005
H	5.0002190	-1.3504682	-0.2540078
H	-5.0002190	1.3504682	-0.2540078
H	5.0002190	1.3504682	-0.2540078
H	-5.0002190	-1.3504682	-0.2540078

Table S24: UPBE0/def2-TZVP structure of $Mn^{IV}O(PF_4^{\bullet})^+$ a_{1u} $^5A_1$.

38

Mn	0.0000000	0.0000000	0.2083834
O	0.0000000	0.0000000	1.8262532
N	1.4077043	-1.4077039	-0.0670955
N	1.4077043	1.4077039	-0.0670955
N	-1.4077043	-1.4077039	-0.0670955
N	-1.4077043	1.4077039	-0.0670955
C	-2.7589289	1.2316385	-0.0563091
C	-1.2316385	2.7589284	-0.0563158
C	-2.4985037	3.4499965	-0.0601081
C	-3.4499967	2.4985038	-0.0601055
C	-3.3847244	0.0000000	-0.0465501
C	-2.7589289	-1.2316385	-0.0563091
C	-3.4499967	-2.4985038	-0.0601055
C	-2.4985037	-3.4499965	-0.0601081
C	-1.2316385	-2.7589284	-0.0563158
C	0.0000000	-3.3847238	-0.0465501
C	1.2316385	-2.7589284	-0.0563158
C	2.4985037	-3.4499965	-0.0601081
C	3.4499967	-2.4985038	-0.0601055
C	2.7589289	-1.2316385	-0.0563091
C	3.3847244	0.0000000	-0.0465501
C	2.7589289	1.2316385	-0.0563091
C	3.4499967	2.4985038	-0.0601055
C	2.4985037	3.4499965	-0.0601081
C	1.2316385	2.7589284	-0.0563158
C	0.0000000	3.3847238	-0.0465501
F	0.0000000	4.7117233	-0.0345118
H	-2.6159069	4.5222795	-0.0638219
H	-4.5222796	2.6159073	-0.0638175
F	-4.7117244	0.0000000	-0.0345595
H	-4.5222796	-2.6159073	-0.0638175
H	-2.6159069	-4.5222795	-0.0638219
F	0.0000000	-4.7117233	-0.0345118
H	2.6159069	-4.5222795	-0.0638219
H	4.5222796	-2.6159073	-0.0638175
F	4.7117244	0.0000000	-0.0345595
H	4.5222796	2.6159073	-0.0638175
H	2.6159069	4.5222795	-0.0638219

Table S25: UPBE0/def2-TZVP structure of $Mn^{IV}O(PF_4^{\bullet})^+$ a_{1u} $^3B_1$.

38

Mn	0.0000000	0.0000000	0.3436389
O	0.0000000	0.0000000	1.8927495
N	0.0000000	2.0048289	0.0502647
N	0.0000000	-2.0048289	0.0502647
N	-1.9365217	0.0000000	-0.1048828
N	1.9365217	0.0000000	-0.1048828
C	1.0737001	-2.8391012	0.0410011
C	-1.0737001	2.8391012	0.0410011
C	1.0737001	2.8391012	0.0410011
C	-1.0737001	-2.8391012	0.0410011
C	-0.6726918	-4.2265230	0.0590792
C	0.6726918	4.2265230	0.0590792
C	-0.6726918	4.2265230	0.0590792
C	0.6726918	-4.2265230	0.0590792
C	2.3784592	-2.3973915	-0.0380955
C	-2.3784592	2.3973915	-0.0380955
C	2.3784592	2.3973915	-0.0380955
C	-2.3784592	-2.3973915	-0.0380955
C	2.7786661	-1.0799969	-0.1259323
C	-2.7786661	1.0799969	-0.1259323
C	2.7786661	1.0799969	-0.1259323
C	-2.7786661	-1.0799969	-0.1259323
C	4.1570254	-0.6728303	-0.2140669
C	-4.1570254	0.6728303	-0.2140669
C	4.1570254	0.6728303	-0.2140669
C	-4.1570254	-0.6728303	-0.2140669
F	-3.3321981	-3.3203658	-0.0496814
F	3.3321981	3.3203658	-0.0496814
F	-3.3321981	3.3203658	-0.0496814
F	3.3321981	-3.3203658	-0.0496814
H	-1.3490391	-5.0668355	0.0555353
H	1.3490391	5.0668355	0.0555353
H	-1.3490391	5.0668355	0.0555353
H	1.3490391	-5.0668355	0.0555353
H	4.9969847	-1.3480780	-0.2596274
H	-4.9969847	1.3480780	-0.2596274
H	4.9969847	1.3480780	-0.2596274
H	-4.9969847	-1.3480780	-0.2596274

Table S26: UPBE0/def2-TZVP structure of $Mn^{IV}O(PF_4^{\bullet})^+$ a_{1u} $^3B_2$.

38

Mn	0.0000000	0.0000000	0.3450592
O	0.0000000	0.0000000	1.8941347
N	0.0000000	1.9373904	-0.1006094
N	0.0000000	-1.9373904	-0.1006094
N	-2.0048765	0.0000000	0.0481764
N	2.0048765	0.0000000	0.0481764
C	1.0799645	-2.7795689	-0.1190768
C	-1.0799645	2.7795689	-0.1190768
C	1.0799645	2.7795689	-0.1190768
C	-1.0799645	-2.7795689	-0.1190768
C	-0.6728281	-4.1583339	-0.2006073
C	0.6728281	4.1583339	-0.2006073
C	-0.6728281	4.1583339	-0.2006073
C	0.6728281	-4.1583339	-0.2006073
C	2.3975464	-2.3788043	-0.0374383
C	-2.3975464	2.3788043	-0.0374383
C	2.3975464	2.3788043	-0.0374383
C	-2.3975464	-2.3788043	-0.0374383
C	2.8392791	-1.0736877	0.0351839
C	-2.8392791	1.0736877	0.0351839
C	2.8392791	1.0736877	0.0351839
C	-2.8392791	-1.0736877	0.0351839
C	4.2267442	-0.6726591	0.0445732
C	-4.2267442	0.6726591	0.0445732
C	4.2267442	0.6726591	0.0445732
C	-4.2267442	-0.6726591	0.0445732
F	-3.3207150	-3.3324043	-0.0494208
F	3.3207150	3.3324043	-0.0494208
F	-3.3207150	3.3324043	-0.0494208
F	3.3207150	-3.3324043	-0.0494208
H	-1.3481257	-4.9984093	-0.2427342
H	1.3481257	4.9984093	-0.2427342
H	-1.3481257	4.9984093	-0.2427342
H	1.3481257	-4.9984093	-0.2427342
H	5.0671147	-1.3489687	0.0359383
H	-5.0671147	1.3489687	0.0359383
H	5.0671147	1.3489687	0.0359383
H	-5.0671147	-1.3489687	0.0359383

Table S27: UPBE0/def2-TZVP structure of $Mn^{IV}O(PF_4^{\bullet})^+$ a_{1u} $^1B_1$.

38

Mn	0.0000000	0.0000000	0.3441129
O	0.0000000	0.0000000	1.8918506
N	0.0000000	2.0061018	0.0482786
N	0.0000000	-2.0061018	0.0482786
N	-1.9358843	0.0000000	-0.1047154
N	1.9358843	0.0000000	-0.1047154
C	1.0737019	-2.8401326	0.0406106
C	-1.0737019	2.8401326	0.0406106
C	1.0737019	2.8401326	0.0406106
C	-1.0737019	-2.8401326	0.0406106
C	-0.6727095	-4.2275738	0.0604430
C	0.6727095	4.2275738	0.0604430
C	-0.6727095	4.2275738	0.0604430
C	0.6727095	-4.2275738	0.0604430
C	2.3782976	-2.3977614	-0.0387825
C	-2.3782976	2.3977614	-0.0387825
C	2.3782976	2.3977614	-0.0387825
C	-2.3782976	-2.3977614	-0.0387825
C	2.7779027	-1.0801370	-0.1261861
C	-2.7779027	1.0801370	-0.1261861
C	2.7779027	1.0801370	-0.1261861
C	-2.7779027	-1.0801370	-0.1261861
C	4.1560909	-0.6728874	-0.2143403
C	-4.1560909	0.6728874	-0.2143403
C	4.1560909	0.6728874	-0.2143403
C	-4.1560909	-0.6728874	-0.2143403
F	-3.3325256	-3.3203260	-0.0505294
F	3.3325256	3.3203260	-0.0505294
F	-3.3325256	3.3203260	-0.0505294
F	3.3325256	-3.3203260	-0.0505294
H	-1.3489676	-5.0680425	0.0582415
H	1.3489676	5.0680425	0.0582415
H	-1.3489676	5.0680425	0.0582415
H	1.3489676	-5.0680425	0.0582415
H	4.9960042	-1.3481403	-0.2602294
H	-4.9960042	1.3481403	-0.2602294
H	4.9960042	1.3481403	-0.2602294
H	-4.9960042	-1.3481403	-0.2602294

Table S28: UPBE0/def2-TZVP structure of $Mn^{IV}O(PF_4^{\bullet})^+$ a_{1u} $^1B_2$.

38

Mn	0.0000000	0.0000000	0.3441257
O	0.0000000	0.0000000	1.8918548
N	0.0000000	2.0061088	0.0482755
N	0.0000000	-2.0061088	0.0482755
N	-1.9358770	0.0000000	-0.1047262
N	1.9358770	0.0000000	-0.1047262
C	1.0737076	-2.8401605	0.0405795
C	-1.0737076	2.8401605	0.0405795
C	1.0737076	2.8401605	0.0405795
C	-1.0737076	-2.8401605	0.0405795
C	-0.6727074	-4.2275911	0.0604652
C	0.6727074	4.2275911	0.0604652
C	-0.6727074	4.2275911	0.0604652
C	0.6727074	-4.2275911	0.0604652
C	2.3782796	-2.3977642	-0.0387975
C	-2.3782796	2.3977642	-0.0387975
C	2.3782796	2.3977642	-0.0387975
C	-2.3782796	-2.3977642	-0.0387975
C	2.7778574	-1.0801228	-0.1261993
C	-2.7778574	1.0801228	-0.1261993
C	2.7778574	1.0801228	-0.1261993
C	-2.7778574	-1.0801228	-0.1261993
C	4.1560668	-0.6728865	-0.2143463
C	-4.1560668	0.6728865	-0.2143463
C	4.1560668	0.6728865	-0.2143463
C	-4.1560668	-0.6728865	-0.2143463
F	-3.3325400	-3.3203294	-0.0505748
F	3.3325400	3.3203294	-0.0505748
F	-3.3325400	3.3203294	-0.0505748
F	3.3325400	-3.3203294	-0.0505748
H	-1.3489606	-5.0680777	0.0583131
H	1.3489606	5.0680777	0.0583131
H	-1.3489606	5.0680777	0.0583131
H	1.3489606	-5.0680777	0.0583131
H	4.9959819	-1.3481421	-0.2602096
H	-4.9959819	1.3481421	-0.2602096
H	4.9959819	1.3481421	-0.2602096
H	-4.9959819	-1.3481421	-0.2602096